ASSESSMENT OF STRUCTURAL INTEGRITY AND POTENTIAL IMPROVEMENTS OF MICRO HYDROPOWER TURBINE

Martin Andreas Just, Gard Sviggum Saabye

June 10, 2013

THE NORWEGIAN UNIVERSITY
OF SCIENCE AND TECHNOLOGY
DEPARTMENT OF ENGINEERING DESIGN
AND MATERIALS

MASTER THESIS SPRING 2013
FOR
STUD.TECHN. GARD SVIGGUM SAABYE
STUD.TECHN. MARTIN ANDREAS JUST

ASSESSMENT OF STRUCTURAL INTEGRITY AND POTENTIAL IMPROVEMENTS OF MICRO HYDROPOWER TURBINE

Vurdering av strukturell integritet og forbedringspotensialer av turbin til mikrovannkraftverk

Remote HydroLight (RHL) is involved in the training, manufacturing and installing of micro-hydropower plants throughout Afghanistan. The NGO helps private workshops and villages to build community owned and maintained electric power plants.

A RHL crossflow turbine (model Hindu Kush) has been subject to fatigue failure of the shaft. Some ad hoc modifications have been made to deal with this issue. It is of interest to see if the modifications can be applied to all turbines of the same type, by assessing the strength and fatigue life of the modified turbine.

The assessment will be performed by finding governing forces by means of flow analysis and material properties from lab testing. The results will be implemented in a Finite Element Analysis (FEA) in order to predict the fatigue life. The results will be used to find potential improvements of the turbine.

The thesis should include the signed problem text, and be written as a research report with summary both in English and Norwegian, conclusion, literature references, table of contents, etc. During preparation of the text, the candidate should make efforts to create a well arranged and well written report. To ease the evaluation of the thesis, it is important to cross-reference text, tables and figures. For evaluation of the work a thorough discussion of results is appreciated.

Three weeks after start of the thesis work, an A3 sheet illustrating the work is to be handed in. A template for this presentation is available on the IPM's web site under the menu

"Masteroppgave" (http://www.ntnu.no/ipm/masteroppgave). This sheet should be updated one week before the Master's thesis is submitted.

The thesis shall be submitted electronically via DAIM, NTNU's system for Digital Archiving and Submission of Master's thesis.

The contact person is Anders Austegard, Remote HydroLight

Torgeir Welo
Head of Division

Bjørn Haugen
Professor/Supervisor

NTNU
Norges teknisk-
naturvitenskapelige universitet
Institutt for produktutvikling
og materialer

Preface

The work presented in this thesis is performed at the Department of Engineering Design and Materials at Norwegian University of Science and Technology. The thesis includes laboratory tests of material used for making a cross-flow turbine to identify material properties and detect defects. The cross-flow turbine is manufactured in Afghanistan based on simplified technical drawings made a NGO called Remote Hydrolight. In addition, a hand calculated flow analysis is conducted with the goal of finding the forces acting on the rotor. These forces are used throughout Finite Element analysis. Ultimately, the goal was to find the fatigue life of the rotor.

These thesis had not been possible without the sparring with each other, and our supervisor professor Bjørn Haugen. His open office-door and technical expertise has been greatly appreciated. It has made the work interesting and exciting in addition to the vast academic learning outcome.

We also have to address a big thank to Anders Austegard from Remote Hydrolight for giving us this challenging project and support with help. His work for better infrastructure in Afghanistan is invaluable.

We would also like to thank Bjørn Andreas Hugaas and Arild Tjernæs of Det Norske Veritas for their invaluable help concerning metallurgical questions. Your help has been greatly appreciated.

The office has been a great place to be this semester, thanks to our fellow students. A give-and-take relationship highly appreciated. Our coffee machine has always been there to crack us up when needed.

Finally, we would like to thank all our friends (especially girlfriends) and family for support and non-technical conversations to clear our heads.

Abstract

A comparative study of two different hydro power turbine designs, made by Remote Hydrolight (RHL) was conducted. The shaft of the first design has suffered from fatigue failures and a bushing was introduced to solve the problem, giving the second design.

In this thesis, flow calculations, finite element analysis (FEA), inspection of micro structures and the weld were carried out, along with fatigue life calculations. This was done for both designs to compare the existing fatigue data with the findings. It was found that the introduction of the bushing is generally beneficial. The stresses at the weld toe previously subject to fatigue fracture were reduced by at least 52,5%.

Two kinds of laboratory activities were carried out in this thesis. Firstly, a metallurgic analysis was performed and unveiled flaws on and in the weld. Micro cracks, cavities and general porosity suggested that the welding procedure also needs to be revised. Such cavities, especially if occurring at the weld toe of the outer rotor disk, may lead to fatigue failure, despite the introduction of the bushing. In addition, a micro Vickers hardness test was conducted. The tests showed that a range of materials are used for making the turbine, with the shaft material having the highest tensile strength.

There exists too few fatigue data's for establishing a fatigue stress limit for the different components. Based on the data received, no reliable fatigue life for the modified turbine with bushing can be calculated.

Sammendrag

Et sammenligningsstudie av to forskjellige mikrovannkraftturbindesign ble gjennomført. Begge design kommer fra Remote Hydrolight (RHL). Akslingen på mange av turbinene av det første designet har gått til utmattingsbrudd. En hylse ble satt på akslingen for å unngå ytterligere utmattingsbrudd, som ga det andre designet.

I denne oppgaven har det blitt gjort strømningsberegninger, Elementanalyse (FEA), undersøkelse av mikrostrukturer og sveis, samt beregninger på utmattingslivet til turbinen. Dette ble gjort på begge design for å kunne sammenligne resultatene med eksisterende utmattingsdata. Det ble konkludert med at innføringen av hylsa var fordelaktig. Spenningen i sveisetåa der de tildligere utmattingsbruddene hadde oppstått ble redusert med minst 52,5%.

To laboratorieundersøkelser ble gjennomført. En metallurgisk undersøkelse ble først gjennomført. Den avdekket feil både i og på sveisen. Mikroskopiske sprekker, tjerver og generell porøsitet anmodet at sveiseprosedyren burde gjennomgås. Tjervene som ble funnet i sveisetåa kan meget lett føre til utmattingsbrudd, selv på hylsa.

Deretter ble det gjennomført Vickers hardhetstesting av de metallurgiske prøvene. Testene viste at det blir brukt forskjellige materialer i byggingen av turbinen, der materialet i akslingen har den høyeste anslåtte strekkfastheten. Det finnes for lite utmattingsdata for å bestemme en utmattingsgrense for de ulike komponentene i turbinen. Med bakgrunn i de mottatte utmattingsdata er det ingen grunnlag for å stadfeste et pålitelig utmattingsliv for den modifiserte turbinen med hylse.

Contents

1 Introduction **1**
- 1.1 The Hindu Kush Turbine (HKT) . . . 1
- 1.2 Background for work . . . 2

2 Theory **6**
- 2.1 Flow through a cross flow turbine . . . 6
  - 2.1.1 Leakage flow . . . 7
  - 2.1.2 Velocity diagrams . . . 8
  - 2.1.3 Efficiency of turbine . . . 9
- 2.2 Forces on turbine blades . . . 11
  - 2.2.1 Torque distribution on individual blades . . . 11
  - 2.2.2 Shaft torque . . . 12
- 2.3 Vickers Hardness test . . . 14
  - 2.3.1 Relationship between hardness, yield- and ultimate tensile strength . . . 14
- 2.4 Governing forces for fatigue analysis . . . 15
  - 2.4.1 Torsion . . . 15
  - 2.4.2 Bending moment . . . 15
  - 2.4.3 Stress distribution . . . 17
  - 2.4.4 Stress Concentration Factor (SCF) . . . 19
- 2.5 Fatigue . . . 20
  - 2.5.1 S-N curve . . . 20
  - 2.5.2 Basquin's equation . . . 20
- 2.6 Finite Element Method . . . 21
  - 2.6.1 Element types and function . . . 21

2.6.2 Constraints 22

3 Lab work **25**
3.1 Weld 25
3.1.1 Qualitative analysis 25
3.2 Metallurgy 27
3.2.1 Acquiring samples 27
3.2.2 Preparation of samples 29
3.2.3 Microscopy and findings 31
3.3 Hardness and strength of material 36
3.3.1 Results 36
3.4 Finite Element Analysis 39
3.4.1 3D Modelling 39
3.4.2 Constraints and boundary conditions 43
3.4.3 Loads 48
3.4.4 Meshing 49
3.4.5 2D models 51

4 Results **52**
4.1 Results flow analysis 52
4.1.1 Forces on turbine blades 52
4.2 Analytical shaft stress calculations 57
4.2.1 Torsion and bending moment 57
4.2.2 Shaft stresses 58
4.3 Results from FEA 60
4.3.1 3D models 60
4.3.2 2D models 64
4.4 Fatigue life 67
4.4.1 Determine slope number b for S-N curve 67
4.4.2 Hand calculations 69
4.4.3 FEA 70

5 Discussion and conclusions **72**
5.1 Discussion 72
5.1.1 Metallurgy 72
5.1.2 Vickers hardness test 73
5.1.3 Flow analysis 73

5.1.4 Shaft stress 74
5.1.5 FEA 74
5.1.6 Fatigue life 77
5.2 Conclusions 79

A Net head - Flow diagram **82**

B Technical Drawings **84**
B.1 Shaft with disks 85
B.2 Shaft dimensions 86
B.3 Disk 87

C Velocity equations **88**

D Colour plots from FEA **90**

E Digital appendix **93**
E.1 Torque distribution on blades 93
E.2 Force calculations 93

List of Figures

1.1 Cross-flow turbine installed in Afghanistan [1] 2
1.2 The fracture surface of a shaft. The turbine in the picture is another, larger model called Pamir Turbine. The failure is however the same for the HKT. 3
1.3 Image of the rotor from the technical drawings supplied by RHL. The bushing is indicated at 6. 4
1.4 Sample of welded bushing connection and sample rod. . . . 5

2.1 Major flow patterns through cross flow turbine 7
2.2 Velocity diagram of flow through rotor 8
2.3 Resultant force on blade 12
2.4 Load on rotor blade [2, p. 37] 13
2.5 Torque distribution on disks in rotor 14
2.6 Figure for calculation of bending moment by beam theory . 16
2.7 Stresses and strains in the shaft 18
2.8 Parameters involved in cyclic stress testing 21
2.9 General S-N curve with effect of crack initiation- and propagation on fatigue life [3] 22
2.10 Two types of linear 3D elements. 23
2.11 An example of a colour plot showing stress distributions in ABAQUS. 23
2.12 Abaqus graphical interface for modelling 24

3.1 Weld on bushing and disk 26
3.2 Initial cut of shaft and bushing 28
3.3 Bushing, shaft and disk sample in resin, Sample 1 28
3.4 Cut-out of shaft, Sample 2 29

3.5 All samples used for the metallographic inspection. 31
3.7 Microstructure of the test rod - Sample 3. 32
3.6 Microstructure of the shaft from Sample 2. 32
3.8 Inclusions in the base material at the root of the weld. . . . 33
3.9 Micro structure in the bushing material 34
3.10 Microcracks in the HAZ. 35
3.11 Vickers hardness testing with Mitutoyo HM-200 36
3.12 Location and numbering for Vickers hardness test points . . 37
3.13 Shaft and disks with partition at blade radius on the left. On the right, partitions to facilitate application of quadrilateral elements inside the part at the disk root. 40
3.14 Cavity in model without bushing. Cavity geometry from b). 41
3.15 Shaft for bushing. 41
3.16 Disk with bushing, cavity on the right. 42
3.17 The assembly of the 2 pulley bushing model. 42
3.18 The assembly of the 1 pulley bushing model. 43
3.19 Overview of all RPs used. 43
3.20 Highlighted areas are constrained in Z-direction. The area constrained with symmetry condition is the cross section surface at the far right end. 2 pulley model without bushing. 44
3.21 Red surface indicates the master surface, the pink is the slave surface. 45
3.22 The two identical parts are tied where indicated to constrain the two parts together the 1 pulley models. 45
3.23 Constraint between reference point and edge. This simulates the behaviour of the turbine bearing. 46
3.24 The pink surface was tied to RP-2. 47
3.25 The indicated surface was coupled to RP-1. 47
3.26 Taken from the 2 pulley bushing model. The flow forces are applied identically in the first 8 models in table 3.5.The dotted lines indicate point load on the opposite side of the disk. a) Flow forces. b) Pulley force applied at reference point, RP-2. 48
3.27 Two alternative load scenarios to introduce both torsional- and bending stresses. R indicates the blade radius. 49

3.28 All stresses were extracted along the paths, starting from the left. a) Old turbine. b) Cavity. c) Bushing. 50

4.1 Torque on blades 54
4.2 Snapshot of rotating runner with blade numbers 55
4.3 Original turbine without bushing Von Mises stress at weld . 60
4.4 Comparison of stresses of one and two pulley configurations of shaft with bushing. 61
4.5 Comparison of stresses of original turbine without bushing with cavity at weld for one and two pulley configuration . . 62
4.6 Comparison of stresses of one and two pulley configurations of shaft with bushing. 63
4.7 Stress distribution for 2D model with bushing cavity. 64
4.8 Stress distribution for 2D model with disk cavity. 65
4.9 Stresses at path for 2 pulley without bushing at 7 meters and 50 meters net head 66
4.10 S-N curve for shaft and bushing material 68
4.11 Comparison of S-N curve for bushing material for different values for slope parameter b 69

D.1 2 pulleys bushing model 90
D.2 2 pulleys model, without bushing 91
D.3 1 pulley cavity model, without bushing 91
D.4 1 pulley broken bushing model 92
D.5 1 pulley bushing model 92

List of Tables

3.1 As Required per AWS A5.1/A5.1M: 2004 26
3.2 Overview of the chemical composition of the deposit material 26
3.3 Results Vickers hardness test 37
3.4 Estimation of ultimate tensile strength 38
3.5 List of models made 39
3.6 The pointloads used for the analyses 49

4.1 Hand-calculated axial- and shear stresses in HKT at weld toe 59
4.2 Relative improvement with introducing of bushing 64
4.3 Nominal- and cavity stresses for the 2D models. 65
4.4 Presentation of hand-calculated fatigue life based on Basquin's equation with b=-0,183 70
4.5 Presentation of fatigue life based on stress levels from FEA with slope value $b = -0,183$ 71
4.6 Presentation of fatigue life based on stress levels from FEA and slope value b=-0,13 71

5.1 Relative SCFs from the 2D analyses. 76

List of Symbols and Abbreviations

Abbreviation	Description
AWS	American Welding Society
FEA	Finite Element Analysis
FEM	Finite Element Method
HKT	Hindu Kush Turbine
NGO	Non-Governmental Organization
RHL	Remote HydroLight
SCF	Stress Concentration Factor
SMAW	Shield Metal Arc Welding
UTS	Ultimate Tensile Strength

List of abbreviations used in this thesis

Symbol	Description	Unit
α	Angle between absolute (C) and peripheral (U) velocity	rad
β	Angle between relative (W) and peripheral (U) velocity	rad
δ	Angle of span turbine blades	rad
η	Efficiency	-
Γ	Hydrolic radius rotor	m
ω	Angular velocity rotor	rad/s
ρ	Density of water	kg/m^3
σ	Axial stress	MPa
τ	Shear Stress	MPa
a	Distance between bearing and outer disk on rotor	m
A	Area	m^2
b	Width of rotor	m
b	Slope parameter S-N curve	-
c	Absolute velocity	m/s
Cu	Tangential component of absolute velocity	m/s
E	Energy of flowing water	J
F	Force	N
g	Gravitatinal acceleration	m/s^2
H_e	Net Head	m
HV	Vickers Hardness	-
I_x	Moment of inertia	m^4
J_{zz}	Torsion constant	m^4
l	Length between bearing in turbine	m
M	Moment	Nm
n	Number of blades in action	-
N	Number of stress cycles	-
Q	Volumetric flow	m^3/s
$R_m^{'}$	Cyclic tensile strength	MPa
R_m	Tensile strength	MPa

List of symbols used in this thesis

Symbol	Description	Unit
R	Radius	m
s	Number of blade spans	-
T	Torque	Nm
u	Peripheral velocity	m/s
v	Water velocity	m/s
w	Relative velocity	m/s
W	Distributed load	N/m
Z	Height	m

List of symbols used in this thesis

Symbol	Description
1	Inlet first stage of cross flow
2	Outlet first stage of cross flow
3	Inlet second stage of cross flow
4	Outlet second stage of cross flow
5	Entrained flow
1→ 2	Stage 1
3→ 4	Stage 2
a	Amplitude
a,e	Equivalent amplitude
b	Bending
bs	Blade span
c	Blade channel
c	Concentration
i	Inner
m	Mean
m,e	Equivalent mean
o	Outer
s	Shaft

List of prefixes, super- and sub scripts used in thesis

Chapter 1

Introduction

For the past few decades, Afghanistan has seen a lot of conflict. The war torn country has a large rural population that have limited access to electricity as the establishment of national infrastructure has been hindered. Supplying electricity to a rural community can be very beneficial for the inhabitants and may help the development of the region. Afghanistan has many valleys and mountains and inevitably many rivers. This makes for a vast potential for the development of hydro power. The ever increasing demand for renewable energy creates yet another incentive to exploit this potential as a mean for the development of the region.

Remote Hydrolight is a non-governmental organisation (NGO) situated in Afghanistan. The NGO helps the local population install, operate and maintain off-grid micro hydro power plants. The components are manufactured locally, with limited access to equipment and high-quality materials. RHL have successfully aided the establishment of over 4000 such plants for over 17 years. More information can be found at the RHL websitet [1].

1.1 The Hindu Kush Turbine (HKT)

HKT is one of the turbine models designed by RHL. The investigated turbine is a cross-flow turbine. They are made after specifications and

drawings by Remote Hydrolight [1]. Because of installation in remote locations without existing infrastructure, the parts has to weight less than 100 kg each because of transport by horses.

Figure 1.1: Cross-flow turbine installed in Afghanistan [1]

HKT is usually installed in old enlarged mill sites to serve electricity to a village. HKT is robust and can cope with various flow conditions and heads and is equipped with either one or two pulleys. Detailed graph for flow range and net head is shown in appendix A. The turbine is connected to a Chinese alternator, delivering up to almost 100 kW under perfect conditions at maximum load.

1.2 Background for work

Several turbines have suffered fatigue failures of the shaft. The fracture has been on the outside weld on the disk as seen in figure 1.2.

Figure 1.2: The fracture surface of a shaft. The turbine in the picture is another, larger model called Pamir Turbine. The failure is however the same for the HKT.

RHL have improved the turbine design by adding a bushing to the shaft. The bushing is made with an inner radius slightly smaller than that of the shaft and heated over an open flame to approximately 300 °C. This expands the bushing enough to fit over the shaft. The bushing is fitted and as the bushing cools and contracts it presses itself on to the shaft. This is called shrink fitting. The bushing is subsequently welded to the disk, as seen in figure 1.3.

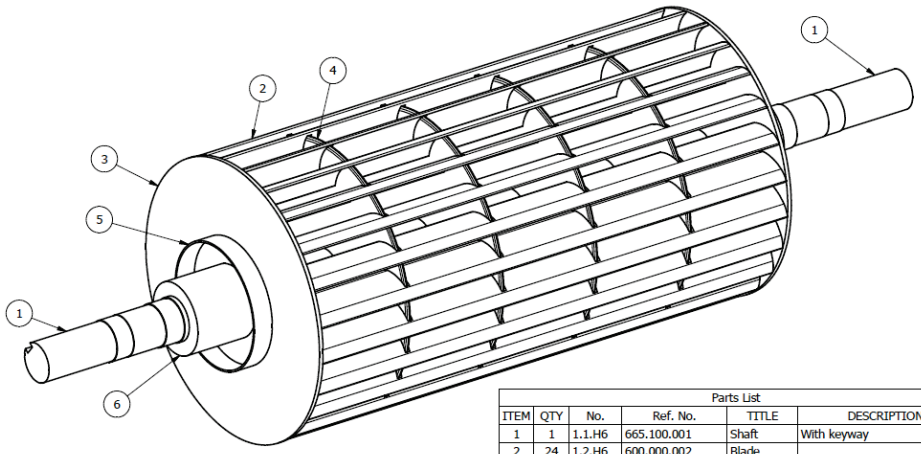

Parts List					
ITEM	QTY	No.	Ref. No.	TITLE	DESCRIPTION
1	1	1.1.H6	665.100.001	Shaft	With keyway
2	24	1.2.H6	600.000.002	Blade	
3	2	1.3.H	665.100.003	Disk	For rotor side
4	4	1.4.H	665.100.004	Disk	Divider
5	2	1.5.H	665.100.005	Seal	HKT water spinner
6	2	1.6.H	600.100.001	Bushing	Shaft reinforcement bushing

Figure 1.3: Image of the rotor from the technical drawings supplied by RHL. The bushing is indicated at 6.

The improvement made to the turbine is rather new. Therefore, RHL do not yet have data on the fatigue life for the turbines with bushings. So far, none of the turbines with bushings have failed from fatigue.

Due to the lack of empirical data, RHL have requested an assessment on the relative improvement of the turbines with the introduction of bushings. In the thesis, the following has been conducted:

- Assessed the changes in stresses by the means of finite element analysis by comparing stresses of the old and new design. This has been done for both 1 and 2 pulleys.
- Inspected the micro structures of the components around the weld to assess the material quality
- Made estimates on expected fatigue life of the components based on FEA results, hardness testing of the components and qualitative evaluations of the influence of micro structure/material quality.
- Assessed the quality of the weld and included this into the qualitative evaluation.

Figure 1.4: Sample of welded bushing connection and sample rod.

RHL sent some samples to use for examination of the turbine components. The two samples were a cut-out of the shaft-disk connection with bushing and a sample rod. They can be seen in figur 1.4.

Chapter 2

Theory

A set of experiments and calculations are carried out in this thesis. The theory presented aims to give a good background for the calculations and experiments. Basic theory for flow through a cross flow turbine is used to find the governing forces acting on the shaft. Fatigue theory presents the background and validity of the equations used in hand-calculation of fatigue life. Theory for Finite Element Method aims to support the Finite Element Analysis.

2.1 Flow through a cross flow turbine

There are two major flow patterns through a cross flow turbine, cross flow and entrained flow shown in figure 2.1.

When water follow the cross flow pattern from point B to D, it hits the turbine blades at two stages before it exits the turbine. Water travels diagonally through the runner after exiting the first stage of the torque transfer at point B. The angle and curvature of the blades are designed so the water will transfer a significant amount of torque at stage two at point D before exiting the turbine.

A part of the flow is trapped by the blades and swung around to the

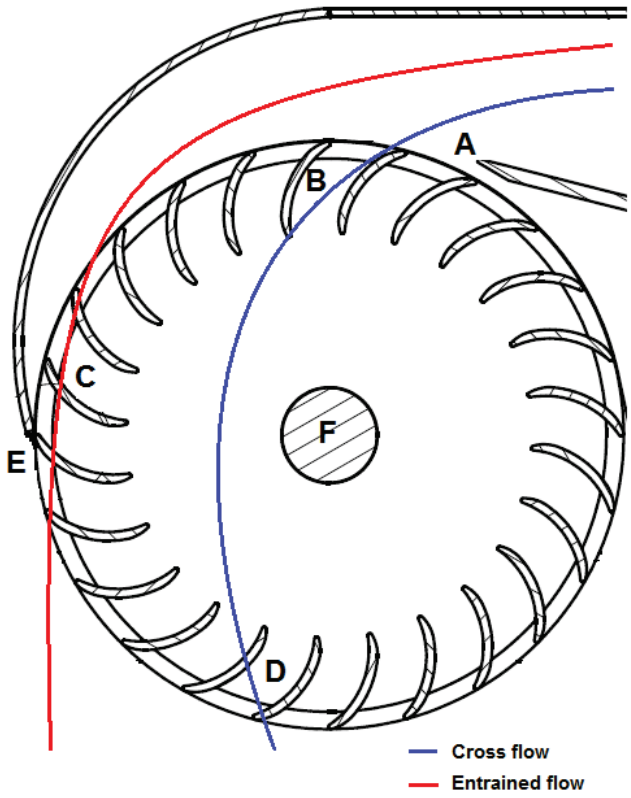

Figure 2.1: Major flow patterns through cross flow turbine

bottom of the turbine. This is what is called entrained flow. This flow pattern will only contribute with one stage of torque transfer.

Rotational speed of the rotor and nozzle opening affects the cross flow through the runner. Inappropriate configuration of the turbine can make the water hit the axle or most of the flow get entrained [2, p. 32].

2.1.1 Leakage flow

Leakage flow is a loss due to water flowing through gaps between the rotor and turbine casing. There are two leakage flows, one between the end of the top cover at point E in figure 2.1. The other leakage flow is between the side casing and the rotor. Lower tolerances in the manufacturing will give less leakage flow.

2.1.2 Velocity diagrams

The flow inside the rotor can be analysed through a one dimensional analysis. The velocity vector from the water flow can be decomposed into a triangle. Each component can be analysed with respect to energy transfer to the rotor. The diagram gives a decent indication of the direction and magnitude of the momentum, making it possible to do hand calculations for an estimation of torque transfer and efficiency. Assuming no leakage flow and no other losses inside the runner, the velocity components from the outlet of he first stage and inlet of the second stage will be the same. Further assumption is that all energy is extracted from the water when leaving the turbine, and cross flow is the only flow pattern.

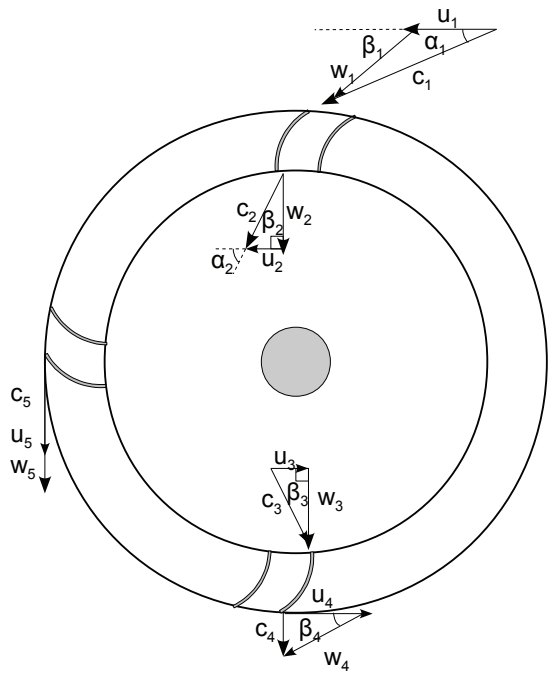

Figure 2.2: Velocity diagram of flow through rotor

The prevailing velocity diagram is shown in figure 2.2 with the following notations;

Subscript 1 - Water entering stage 1

Subscript 2 - Water leaving stage 1

Subscript 3 - Water entering stage 2

Subscript 4 - Water leaving stage 2

Subscript 5 - Entrained flow

W - Relative velocity

C - Absolute velocity

U - Peripheral velocity, runner velocity

α - Angle between absolute and peripheral velocity

β - Angle between relative and peripheral velocity and between the tangent of the blade curvature and runner periphery

2.1.3 Efficiency of turbine

The efficiency of the turbine is defined as the ratio between the power output from the turbine to the generator and the energy of the water flowing into the turbine. When all the energy from the water is utilized and transferred into movement of the rotor, the ratio will be equal to one which means an efficiency of 100%.

$$\eta = \frac{E_{utilized}}{E_{available}} = \frac{E_a - loss}{E_a} \tag{2.1}$$

Efficiency can also be expressed as power output divided by available power. The power output from the turbine is calculated by measuring the shaft torque and multiplying it with the angular velocity of the rotor.

$$\eta = \frac{T_s \omega}{\rho g Q H_e} \tag{2.2}$$

The variables and constants for equation 2.2;

T_s - Shaft torque, Nm

$\boldsymbol{\omega}$ - Angular velocity shaft, rad/s

$\boldsymbol{\rho}$ - Density of water, kg/m^3

g - Gravitational acceleration, m/s^2

Q - Volumetric flow rate of water, m^3/s

H_e - Net head, m

There are some quantities that has to be measured. Shaft torque and angular velocity is measured directly from the shaft. Volumetric flow rate is measured with a flow meter from the turbine inlet. Net head is calculated with use of equation 2.3.

$$H_e = \frac{v_1^2 - v_2^2}{2g} + \frac{\Delta p}{\rho g} + Z \tag{2.3}$$

The governing variables for calculating net head;

v_1 - Water velocity at turbine inlet, m/s

v_2 - Water velocity at turbine outlet, m/s

Δp - Pressure difference between inlet and outlet of turbine, Pa

Z - Difference in elevation between reservoir and runner, m

To calculate the theoretical efficiency of the turbine, the shaft torque T_s can be estimated based on a flow analysis presented in section 2.2.2. The angular velocity of the rotor, ω, is set to be equal to the tangential flow velocity at inlet, U.

$$\omega = \frac{20\sqrt{H_e}}{R_o} \cdot \frac{2\pi}{60} \tag{2.4}$$

R_o is the radius from the centre of the rotor to the outer edge of the turbine blades.

2.2 Forces on turbine blades

Forces from the flowing water acting on the turbine blades to set the runner into movement. The maximum force acting on one blade can be calculated with use of the velocity vectors of the water and the geometry of the runner. A study by P.Verhaart [4] has been carried out to calculate the forces acting on the blades to prevent fatigue failure.

The torque transmitted by a blade channel is given by momentum theory;

$$T_{c1\to 2} = Q_c\,\rho(c_1 R_o cos\alpha_1 - u_2 R_i) \tag{2.5}$$

$T_{c1\to 2}$ - Torque transmitted by blade channel from stage 1, Nm

Q_c - Volumetric flow through blade channel, m^3/s

R_o - Outer radius, from center of the runner to outer edge of blades, m

R_i - inner radius, from center of the runner to inner edge of blades, m

$$F = \frac{T_c}{\Gamma} \tag{2.6}$$

To find the centric force acting in the middle of the blade curvature, T_c from equation 2.5 is divided by the distance Γ from the middle of the blade curvature to the centre of the runner, shown in figure 2.3 on the following page.

$$\Gamma^2 = R_i^2 + (2R_{bs}sin(\delta/4))^2 - 4R_i R_{bs} sin(\delta/4)cos(\pi - \delta/4) \tag{2.7}$$

2.2.1 Torque distribution on individual blades

An investigation of how the torque is transferred from the water to the turbine with respect to contribution for each individual blade is done by Walseth [2]. An uncalibrated strain gage was used to find the percentage of torque contributed by the two stages. The strain gage was attached to the backside of a turbine blade, and the voltage was presented in a

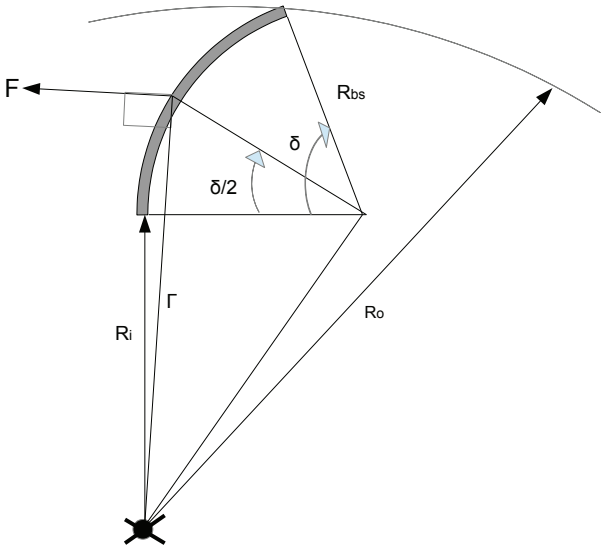

Figure 2.3: Resultant force on blade

graph. This graph and the overall efficiency could be used to scale the graph representing the torque contribution by each blade channel. The maximum force on the blades will be used as a scaling factor for the maximum point on figure 2.4. The first peak in the mentioned figure represent the first stage in the cross-flow torque transfer, while the second peak represent the second stage.

2.2.2 Shaft torque

The blades are welded to disks which again are welded to the axle. The disks are placed evenly on the blades. This means less torque is transferred through the two outer disks, illustrated in figure 2.5 on page 14, where T_s is the total amount of shaft torque.

To estimate the total amount of torque transferred to the axle, and the

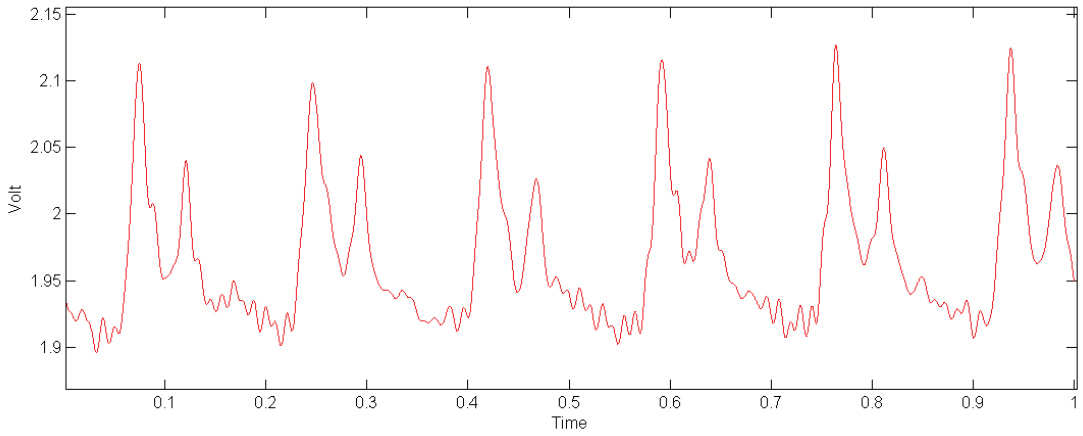

Figure 2.4: Load on rotor blade [2, p. 37]

efficiency of the turbine, the torque from stage 1 and 2 is summed. To simplify the calculation, it is assumed that all the available water follows the cross-flow pattern. A further assumption based on the geometry of the construction is that 8 blades contribute with torque transfer simultaneously in stage 1 of the cross-flow, and 8 in stage 2. This is a conservative assumption, as it is expected to give greater forces.

$$T_{c3\to4} = Q_c R_{bs}(u_3 R_i - Cu_4 R_o) \tag{2.8}$$

Here Cu_4 is the tangential component of the absolute velocity (c_4). This term can be neglected assuming the water has no rotational energy as it leaves the rotor.

The total amount of torque transferred to the shaft is then given by equation 2.9, where n is the number of blades transferring torque in each stage.

$$T_s = nQ_c R_{bs}((c_1 R_o cos\alpha_1 - u_2 R_i) + u_3 R_i) = n(T_{c1\to2} + T_{c3\to4}) \tag{2.9}$$

To calculate the different velocities, the equations from Appendix C are used. The known inputs are the geometry of the runner and the inlet velocity set to be equal to c_1.

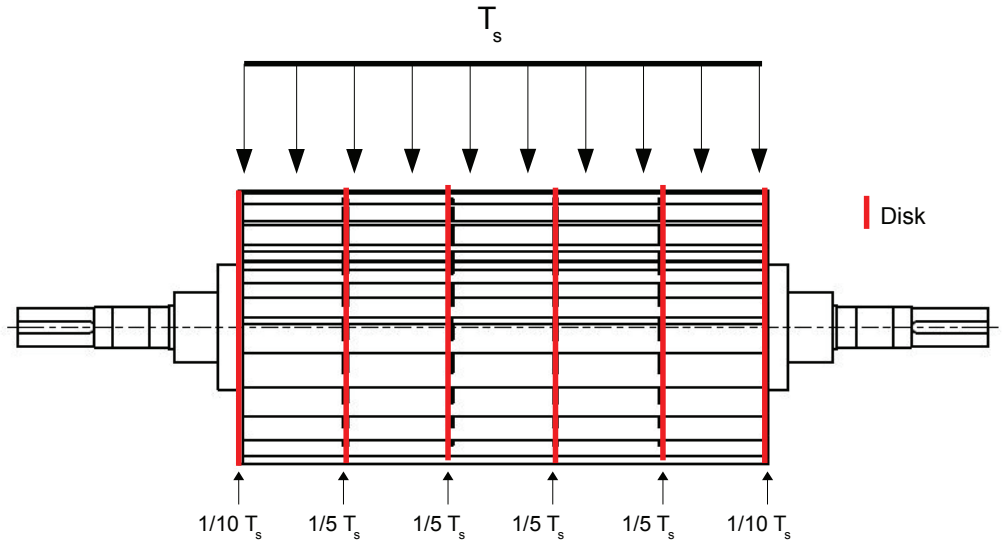

Figure 2.5: Torque distribution on disks in rotor

2.3 Vickers Hardness test

Vickers hardness is a parameter and method for measuring hardness of a material. The test is non-destructive, and involves poking the material using a pyramidal tip with a certain force. The area of the crater formed by the tip is measured, follows the equation $HV = \frac{F}{A}$, where HV is the Vickers hardness, F is the applied force in kilograms and A is the area of the crater. The hardness is denoted xxHVyy where xx is the hardness number, HV tells that it is in Vickers hardess, and yy is the applied force in kilograms.

2.3.1 Relationship between hardness, yield- and ultimate tensile strength

According to Zhang [5] based on experimental results, the relationship between hardness, yield- and ultimate tensile strength can be written as in equation 2.10. σ_y is yield strength in MPa and σ_{UTS} is ultimate tensile

strength of the material in MPa.

$$0,3\sigma_y < HV < 0.3\sigma_{UTS} \tag{2.10}$$

This will be a conservative assumption, as the estimated tensile strength will be lower than the real tensile strength.

2.4 Governing forces for fatigue analysis

2.4.1 Torsion

The shaft torque acts as a cyclic load, given that the turbine acts as an impulse turbine [6, p.33]. The mean value will be above zero as the shaft is rotating continuously in one direction. Torsion is a result of a twisted shaft due to applied torque. Because of the cross-flow nature, each blade contributes with two stress peaks within one revolution.

2.4.2 Bending moment

Both the pulley and the forces from the rotor contributes to the bending of the shaft.

Pulley forces

The turbine is equipped with either one pulley, or one pulley on each side depending on available head (H_e) and flow (Q). The pulleys causes the shaft to bend, introducing bending moment in the shaft. The force from the pulley acting on the shaft is modelled as a point load, F, shown in figure 2.6.

Flow forces

The forces on the turbine blades contributes with bending moment to the shaft. It acts in the opposite direction of the bending moment contributed

by the pulley. The bending contribution on the shaft from the flow forces can be modelled with classic beam theory as a distributed load, W, shown in figure 2.6. Originally, the forces from the blades to the shaft is transferred through five disks. This assumption of a distributed load can be made because the point of interest lies outside the loaded area.

Equations

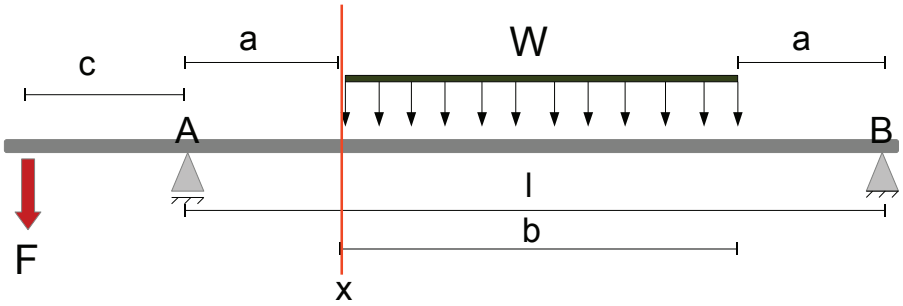

Figure 2.6: Figure for calculation of bending moment by beam theory

Point x in figure 2.6 represent the point where fracture of the shaft has occurred. It is in the weld toe of the outer disk of the rotor. The pulley force F and flow force W contributions to bending moment are calculated separately and combined with the use of the super position principle. When the upper side of the beam in figure 2.6 is defined as tension side, the bending moment from the flow forces W will have a negative sign.

The contribution of bending moment in point x from the pulley force F is shown in equation 2.11

$$M_b^F = \frac{Fc(a+b)}{l} \tag{2.11}$$

The contribution of bending moment in point x from the flow forces W is shown in equation 2.12

$$M_b^W = \frac{Wba}{2} \tag{2.12}$$

The combined bending moment in point x will then be as in equation 2.13.

$$M_b = \frac{Fc(a+b)}{l} - \frac{Wba}{2} \tag{2.13}$$

In the case where the shaft is connected to one pulley on each side, the total bending moment in point x will be as in equation 2.14

$$M_b = \frac{Fc(2a+b)}{l} - \frac{Wba}{2} \tag{2.14}$$

2.4.3 Stress distribution

The bending and torsion on the shaft results in a biaxial stress distribution. The bending contributes with axial stresses (tension and compression) normal to the cross section of the shaft. Torsion contributes with shear stress coplanar with the shaft cross section.
The point of interest is at weld toe on tension side at point x from figure 2.6 on the preceding page.

The tension stress from bending at the weld toe will be;

$$\sigma = \frac{M_b r}{I_x} = \frac{4M_b}{\pi r^3} \tag{2.15}$$

M_b is the bending moment found in equation 2.13 or 2.14, I_x is the moment of inertia for the circular cross-section of the shaft and r is the radius of the shaft at the weld toe.

The shear stress caused by torsion of the shaft is at it's maximum at the outer surface of the shaft, where the weld toe in point x from figure 2.6 is located. Torsion is a consequence of torque, and is calculated for the Hindu Kush Turbine in section 2.2.2 equation 2.9. The shear stress caused by torsion is given by equation 2.16.

$$\tau = \frac{Tr}{J_{zz}} = \frac{2T_s}{\pi r^3} \tag{2.16}$$

T_s is the applied torque to the shaft in Nm, J_{zz} is the torsion constant for a round, solid shaft where r is the radius of the shaft at the weld toe.

Stress amplitude and mean stress

The two most important stress parameters when determining fatigue life is the stress amplitude σ_a and mean stress σ_m illustrated in figure 2.8. The stress situation is biaxial, as shown in figure 2.7. Stress situation is assumed proportional, which means that the relationship between the different stress amplitudes (σ_a and τ_a) and the mean stresses (σ_m and τ_m) are constant.

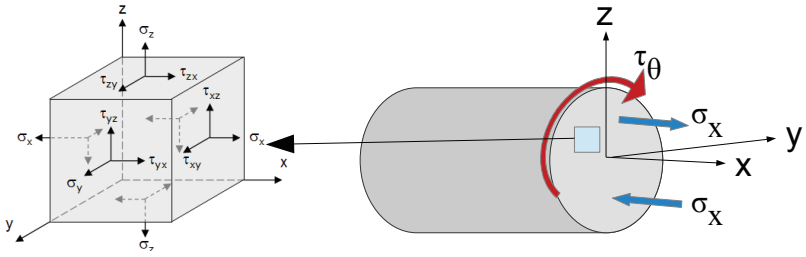

Figure 2.7: Stresses and strains in the shaft

In order to estimate the fatigue life by hand calculations, the equivalent stress follows von Mises criterion [7, p. 285]. This implies that the multi-axial stress situation can be calculated as a one-axial stress distribution. The material is ductile, and the crack initiation and propagation follows from cyclic plastic deformation. Crack initiation and propagation force is governed by the equivalent stress amplitude.

$$\sigma_{a,e} = \sqrt{\sigma_{xa}^2 + 3\tau_{xya}^2} \tag{2.17}$$

$\sigma_{a,e}$ means the equivalent stress amplitude. The stress caused by bending is fully reversed within one cycle, as the shaft rotates. The point in tension will half a period later be in compression. Because of the fully reversed nature of the cyclic stress caused by bending of the shaft, the mean bending stress is zero. The stress amplitude will be σ_{max}, as the stress level oscillates from σ_{max} to $\sigma_{min} = \sigma_{-max}$.

Shear stresses in the shaft caused by torsion will mainly be constant, as the load and rotational speed of the shaft varies marginally within one load cycle. The blades position relative to the nozzle changes with

rotation. When the blades are optimally alligned with the flow, more torque is transferred to the shaft, hence the "jerk" in shear stresss. The maximum shear will be obtained with the amount torque as follows from the contribution from 8 blades inserted in equation 2.16. Minimum shear follows from the contribution of torque from the number of blades making the average amount of torque match the efficiency of 78,6% for the turbine found by Walseth [2].

When the turbine is set up with 2 pulleys, half of the torsion is taken up by each pulley. This implies that half of the total torque causing shear stress in the point of interest (point x in figure 2.6 on page 16)

When it comes to mean stresses, *Sines' rule* is used to find the equivalent mean stress [8, sec. 2.6.2]. Experience has shown that pure torsion has little or no effect on the equivalent mean stress. This is implied in Sine's rule as follows in equation 2.18. $\sigma_{m,e}$ means equivalent mean stress.

$$\sigma_{m,e} = min\{\sqrt{\sigma_{zm}^2 + 3\tau_{xym}^2}, \sigma_{xm} + \sigma_{ym}\} \tag{2.18}$$

2.4.4 Stress Concentration Factor (SCF)

The point of interests (point x in figure 2.6 on page 16) sits at a discontinuity. At discontinuities, the stress will be higher than in the areas around. The stress concentration factor is a measure of the stress at the discontinuity divided by the stress a distance from the discontinuity (equation 2.19). In the case for the turbine, the discontinuity is a fillet weld.

$$SCF = \frac{\sigma_c}{\sigma_{m,e} + \sigma_{a,e}} \tag{2.19}$$

$\sigma_{m,e} + \sigma_{a,e}$ is the surface stress some distance from the discontinuity, and σ_c is the concentrated stress at the weld toe. Surface finish, geometry, load conditions and micro structure of the material affects the concentration of stress in a point. The only way of getting the correct SCF for a complex loading situation and geometry is through testing or FEA. Some estimations may still be made based on existing tables.

2.5 Fatigue

When a structure is subject to a cyclic load, fatigue fracture can occur even when the resulting stressess are below yield strength of the material [3, p. 1]. The fatigue life of a structure or component is a prediction of the number of stress cycles before failure. There is several factors affecting the fatigue life, including metallurgic composition of the material, stress state, stress level and cyclic load behaviour.

The development of a fatigue fracture is divided into two stages, *fatigue crack initiation* and *fatigue crack propagation*. Firstly, a crack is initiated due to repeated loading and unloading. The crack is formed in regions where stress is most severe and where there are structural defects. Then the crack propagates, accelerating around microscopic nucleations in the material, until the cross section is unable withstand the load and ends up with total fracture.

2.5.1 S-N curve

In case of high-cycle fatigue situations, an S-N curve is used to describe the number of cycles to failure. The stress S (or σ) is plotted against the number of cycles (N) to fracture at a logarithmic scale. The stress parameter could have the form of either the difference between the maximum and minimum stress ($\Delta\sigma = \sigma_{max} - \sigma_{min}$), mean stress ($\sigma_m = (\sigma_{max} + \sigma_{min})/2$) or the stress amplitude ($\sigma_a = (\sigma_{max} - \sigma_{min})/2$) all illustrated in figure 2.8.

At low stresses, the fatigue limit line becomes horizontal for some engineering materials, which means the stress level is below the fatigue limit and the component has infinite fatigue life.

2.5.2 Basquin's equation

Basquin's equation is an approach for describing the slope of the S-N curve. Assuming the slope of the S-N curve is linear when the number of cycles N on the x-axis is logarithmic, the constant slope gradient is b. This is only valid for N below the fatigue limit. The Basquin equation

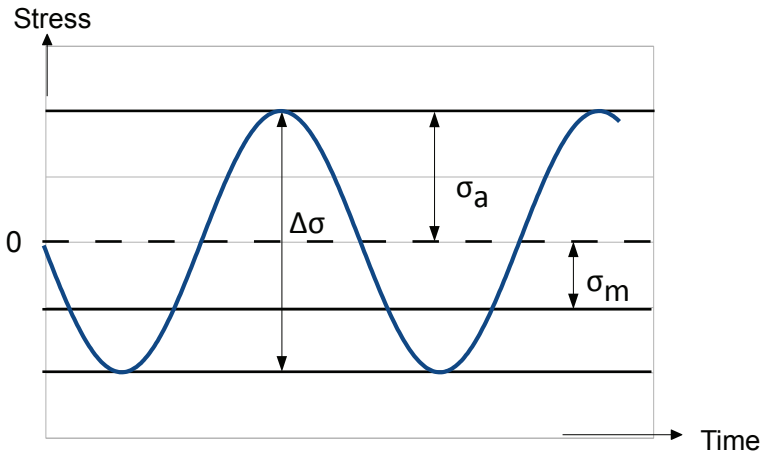

Figure 2.8: Parameters involved in cyclic stress testing

(2.20) states the allowed stress amplitude σ_a based on the cyclic tensile strength $R_m^{'}$ of the material, number of cycles N and the slope gradient b [8, p. 12].

$$\sigma_a = R_m^{'}(2N)^b \tag{2.20}$$

A modification done by Morrow allows for including mean stresses in Basquin's equation, which can contribute to reducing the fatigue life significantly. The modification is shown in equation 2.21.

$$\sigma_a = (R_m^{'} - \sigma_m)(2N)^b \tag{2.21}$$

2.6 Finite Element Method

2.6.1 Element types and function

The Finite Element Method (FEM) is a numerical method for solving boundary value problems. In this thesis, it is used for a complex structure with multi axial loading and stresses. The continuous structure is divided into a finite number of elements of a certain geometry. The elements used

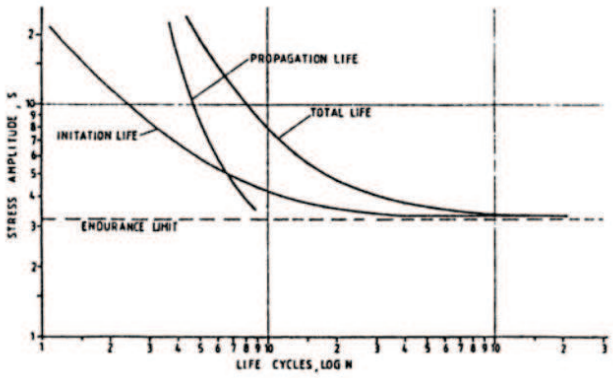

Figure 2.9: General S-N curve with effect of crack initiation- and propagation on fatigue life [3]

in the analyses were 4 node terahedral and 8 node hexahedral, as seen in figure 2.10.

The nodes transfer displacements from one element to the other elements sharing the same nodes. The node values are interpolated through the element by an interpolation function. For these kinds of elements, these functions are linear. This renders a displacement field for the whole model, hence the strains and stresses.

The element size is analogous to the step size in numerical iteration - smaller elements render more exact results, but require more calculation time. The finite elements sotware, ABAQUS, was used for all 3D modelling and analyses. [9]

2.6.2 Constraints

A *structural distributing coupling* in ABAQUS constrains a part of the geometry to a reference point or node. Usually, a surface, an edge or a set of nodes are coupled. This area is then constricted to the degrees of freedom of the reference. The area is allowed to deform, but the *sum* of the displacements are zero relative to the reference.

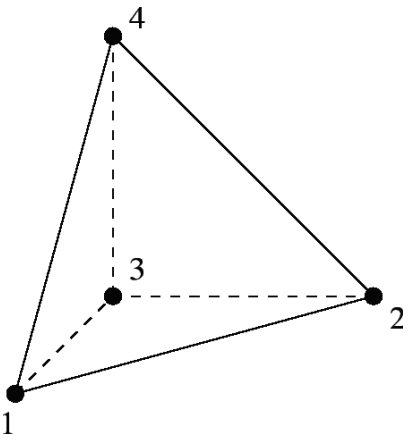

(a) A 4 node tetrahedral element with linear interpolation functions.

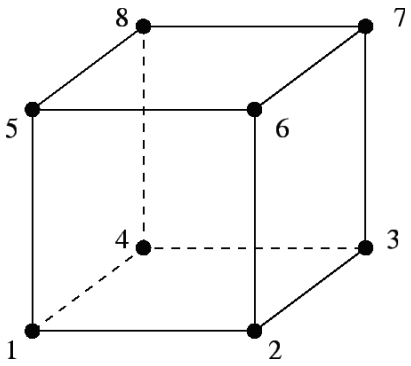

(b) An 8 node hexahedral element, also linear.

Figure 2.10: Two types of linear 3D elements.

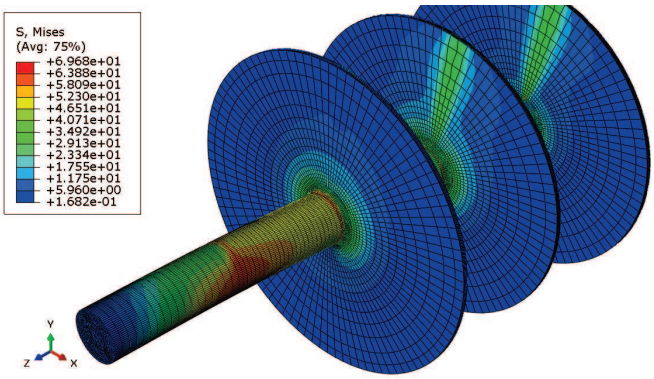

Figure 2.11: An example of a colour plot showing stress distributions in ABAQUS.

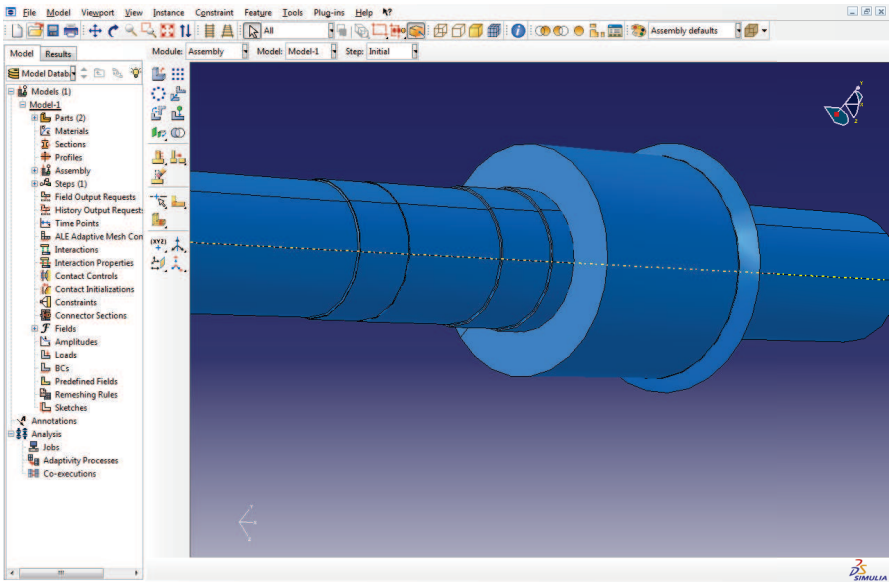

Figure 2.12: Abaqus graphical interface for modelling

Chapter 3

Lab work

Testing was carried out in order to get input data for calculations as well as the qualitative assessment. Metallography and hardness testing of samples was conducted in the Metallurgic Lab at the Department of Engineering Design and Materials at NTNU.

3.1 Weld

Chinese welding rods of carbon steel is used in all welds throughout the turbine and runner. The welding process is called Shield Metal Arc Welding (SMAW) and is known to be very versatile. The rod is certified American Welding Society (AWS) E6013, where 60 meaning 60 Ksi (430MPa) tensile strength, and 13 denotes basic coating type and ability to take both AC and DC current. The weld is said to have following properties [10];

The material composition of the weld deposit is shown in table 3.2.

3.1.1 Qualitative analysis

A wreckage of the shaft with bushing and disk is used in qualitative analysis of the welding. The weld connects the bushing with the disk where

Length rod	350 mm
Diameter rod	3,2 mm
Yield Strength	330 MPa
Tensile Strength	430 MPa
Elongation	min 17%
Current (AC or DC)	110 - 140 A

Table 3.1: As Required per AWS A5.1/A5.1M: 2004

Chemical composition of deposit material						
% C	%Mn	%Si	%Ni	%Cr	%Mo	%V
0,2 max	1,2 max	1,0 max	0,3 max	0,20 max	0,3 max	0,08 max

Table 3.2: Overview of the chemical composition of the deposit material

the rotor blades are connected.

Figure 3.1: Weld on bushing and disk

Quality issues were seen on the weld. These can be seen in figure 3.1 and are listed below [11];

Porosity Small cavities or holes resulting from gas pockets in weld metal. Possible causes could be dirty work piece, arc length to long and/or damp electrode. Corrective actions is to ensure clean welding surfaces, reduce arc length and/or use dry electrode.

Excessive penetration Weld metal melting through base metal and hanging underneath weld. Possible causes could be excessive heat input or wrong welding technique. Corrective actions is to select lower amperage, use smaller electrode and/or adjust travel speed.

Heat Affected Zone (HAZ)

The HAZ is the are between the weld and base material in a welded structure. The micro structure here differs from both base- and weld structure. As a result of the high temperature during welding and the subsequent cooling, the structure here becomes quite different. Cracks may occur as a result of the temperature expansion and contraction as well as the potential brittleness. [12]

3.2 Metallurgy

A series of laboratory tests were performed to assess the condition of the materials of the components and weld. The micro structure was inspected to find possible flaws or defects in the materials and weld.

3.2.1 Acquiring samples

Three samples were acquired from the components for micro structure analysis.

Weld

Firstly, the turbine shaft and bushing were cut using an electrical saw with cooling liquid, figure 3.2 , giving the basis for the weld sample.

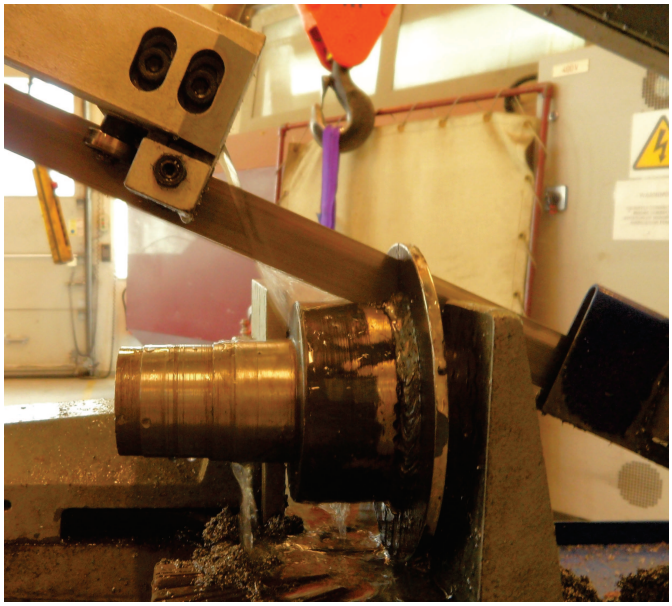

Figure 3.2: Initial cut of shaft and bushing

Secondly, the excessive metal was trimmed manually, using a conventional hack saw. Thirdly, the sample was cut to fit the mounting chamber. This was done using an automatic diamond disc cutter. All sharp corners and edges were subsequently rounded with sand paper to prevent the mounting resin from cracking. This sample is hereby denoted Sample 1, seen in figure 3.3. The sample contains some material from weld deposit, bushing and disk.

Figure 3.3: Bushing, shaft and disk sample in resin, Sample 1

Shaft

The shaft sample was cut manually with a conventional hack saw. Two diagonal cuts were made to extract the sample as seen in figur 3.4. All sharp corners and edges were subsequently rounded with sand paper to prevent the mounting resin from cracking. This sample is hereby denoted Sample 2.

Figure 3.4: Cut-out of shaft, Sample 2

Rod

The rod was cut using a large diamond disc cutter with cooling liquid. The sample was not mounted, but sharp edges were rounded to prevent cutting fingers while grinding. This sample is hereby denoted Sample 3.

3.2.2 Preparation of samples

To obtain photographs of the micro structure, samples need to be ground, polished and etched before put under the microscope.

Mounting

Samples 1 and 2 were too small to hold on the grinding disks and were therefore mounted. The samples were cleaned and lowered into the mounting chamber. 30 and 20 ml of M03012 resin was used for samples 1 and 2, respectively. The heating time was set to 1:30 min. and the cooling time was set to 3:00 min. The chamber pressure was set to 290 bar.

Grinding

Grinding is performed to smooth the surface of the sample. An electrically powered grinding disks covered in sandpaper that are continually sprayed with water was used for grinding. The water cools the sample down, as well as hindering airborne metallic and plastic dust. All samples were ground using sandpaper with 220, 500, 800, 1200 and 2500 grit, successively. While changing paper on the grinding disks, the samples were kept in ethanol to avoid pitting corrosion of the surfaces. After grinding, the samples were cleaned ultrasonically to remove any debris that might damage the sample during polishing.

Polishing

All samples were polished manually on rotating disks with $3\mu m$ and $1\mu m$ pads. The disks were sprayed with Struers DP-Spray P and lubricant. The samples were ultrasonically cleaned going from $3\mu m$ to $1\mu m$ to avoid contamination of the disks with coarser particles. Contamination may lead to scratches on the samples, compromising the quality of the eventual pictures.

Etching

In order to bring out the micro structure of steel, the samples must be etched. The phases in the material react differently to the etchant, giving them different colours. This allows for an examination of the micro structure. All samples were etched in a 2 % nital solution (pure ethanol with

2 % nitric acid) for approximatively 10 seconds, separately. After etching the samples were quickly rinsed in running water and cleaned with ethanol to avoid further etching. The readily prepared samples are seen in figure 3.5.

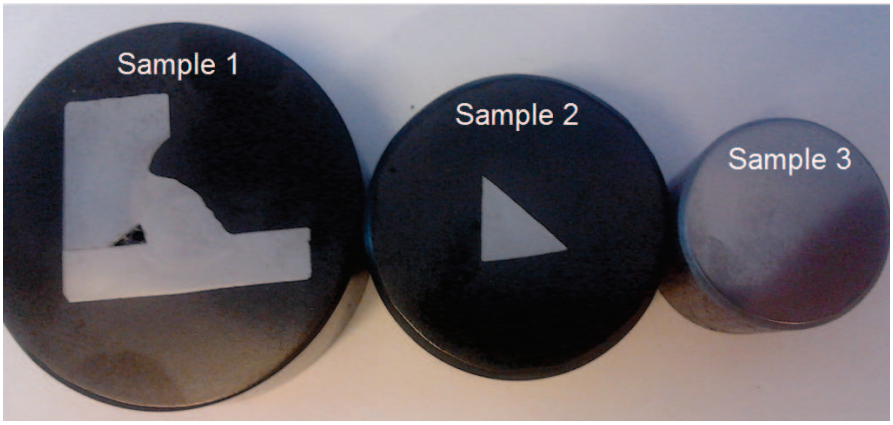

Figure 3.5: All samples used for the metallographic inspection.

3.2.3 Microscopy and findings

All samples were examined in a light microscope. Potential flaws, defects or inclusions in the materials that might be detrimental to the material quality were things to look out for.

Findings

All samples showed a ferritic - pearlitic structure, as expected, however varying in pearlite content. In figure 3.6 the light areas are ferrite, the dark are pearlite. All materials had a fairly high number of inclusions, most likely MnS (manganese sulphides) [12]. These can be seen in figure 3.7. The grain sizes in the different samples varied substantially. This difference is easily observed in figure 3.6 and figure 3.7. The structure in figure 3.7 seems to have less inclusions than the one in figure 3.6. The images were taken from Sample 2 and 3, respectively.

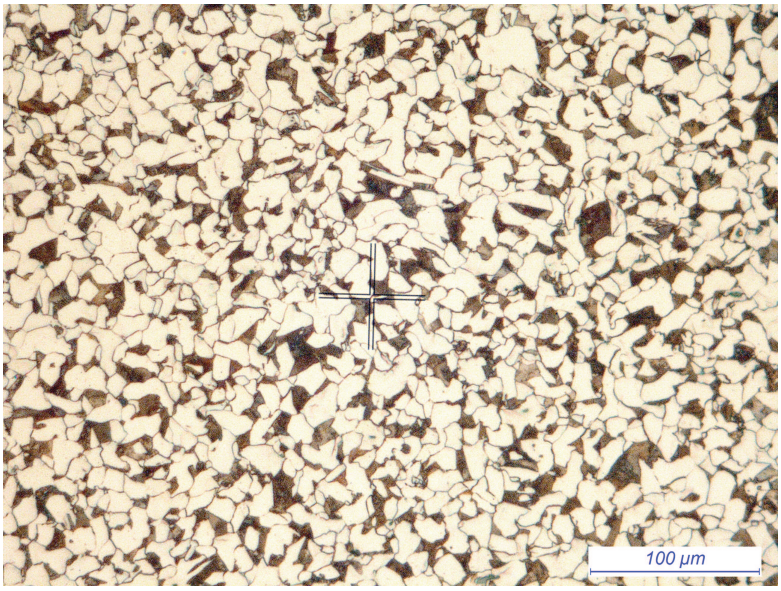

Figure 3.7: Microstructure of the test rod - Sample 3.

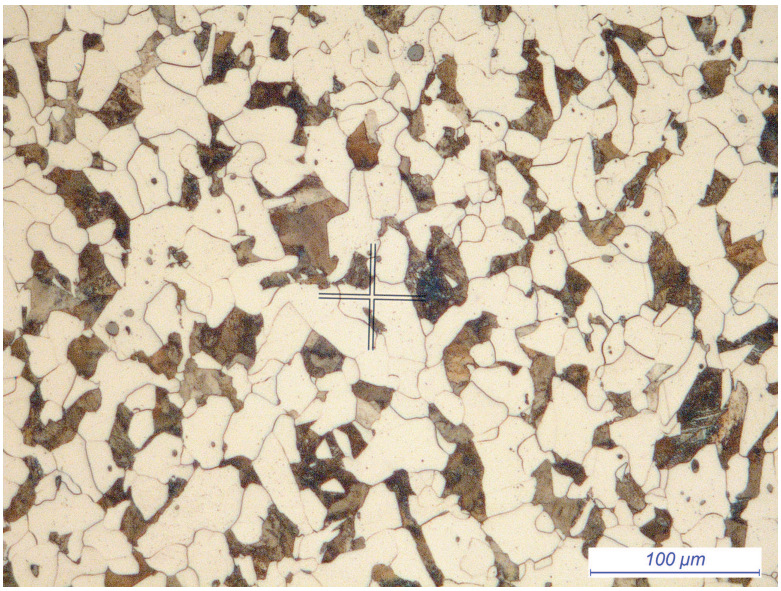

Figure 3.6: Microstructure of the shaft from Sample 2.

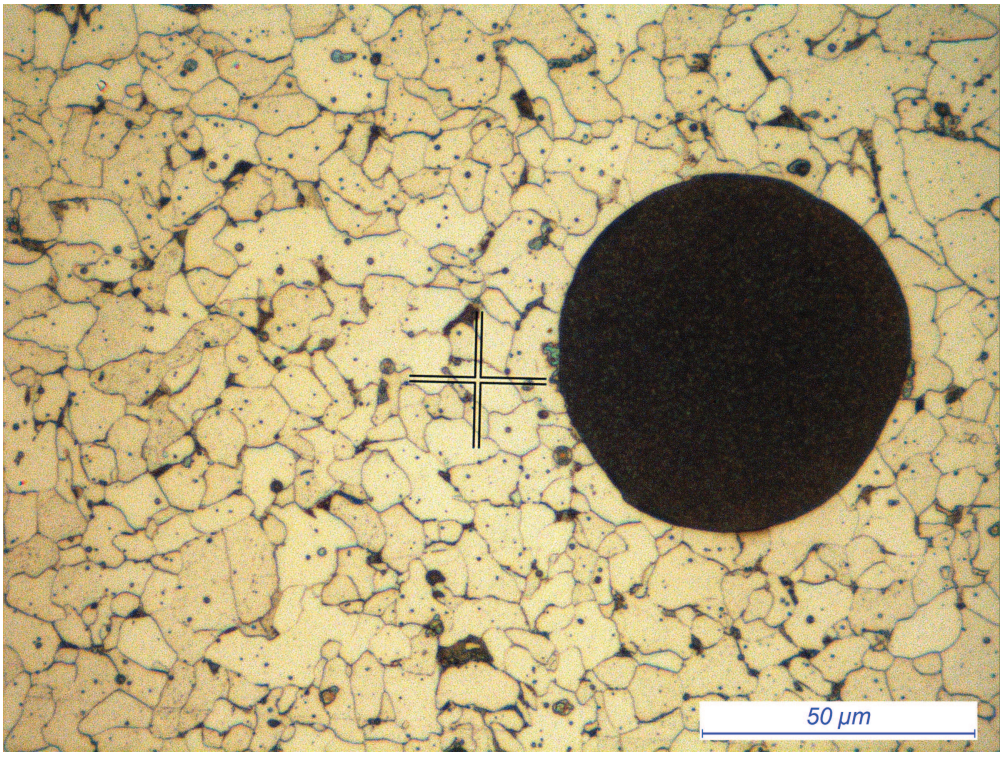

Figure 3.8: Inclusions in the base material at the root of the weld.

In figure 3.8 a very large inclusion is visible. This is most likely an oxide. Many small inclusions are also present. As with the previous, these are most likely MnS. There is very little pearlite present in this micro structure. The image is taken from Sample 1.

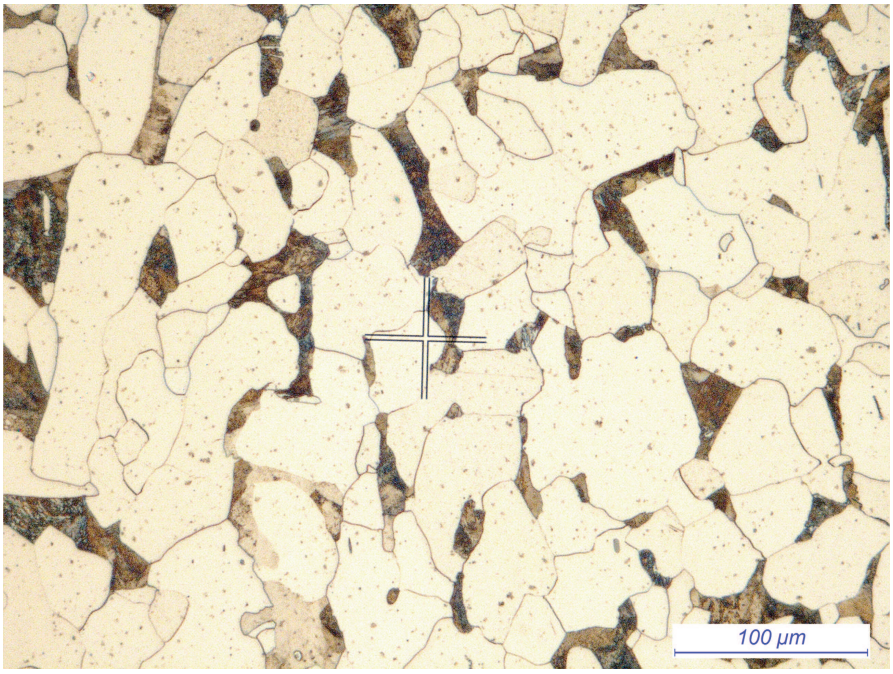

Figure 3.9: Micro structure in the bushing material

The bushing has the largest grain size of all the samples. It has a low pearlite content, which is seen in figure 3.9. Small inclusions of what is most likely MnS. Image taken from Sample 1.

Figure 3.10: Microcracks in the HAZ.

On the bushing side of the HAZ, there was found micro cracks, as seen in figure 3.10. The cracks are up to 0.1 mm in length. Image taken from Sample 1.

3.3 Hardness and strength of material

In order to estimate the strength of the different materials, a Vickers hardness test is performed. There is an empirical correlation between the hardness of the material and the yield and ultimate tensile strength [5].

3.3.1 Results

Vickers Hardness Test

A Vickers hardness test was conducted using a micro Vickers hardness testing machine of type Mitutoyo HM-200. The samples from the metallography were tested in order to estimate the material properties of the different components. Twelve points were investigated, two for each area of interests. The numbering and locations of the points are shown in figure 3.12 on the following page. The applied force was 1 kg.

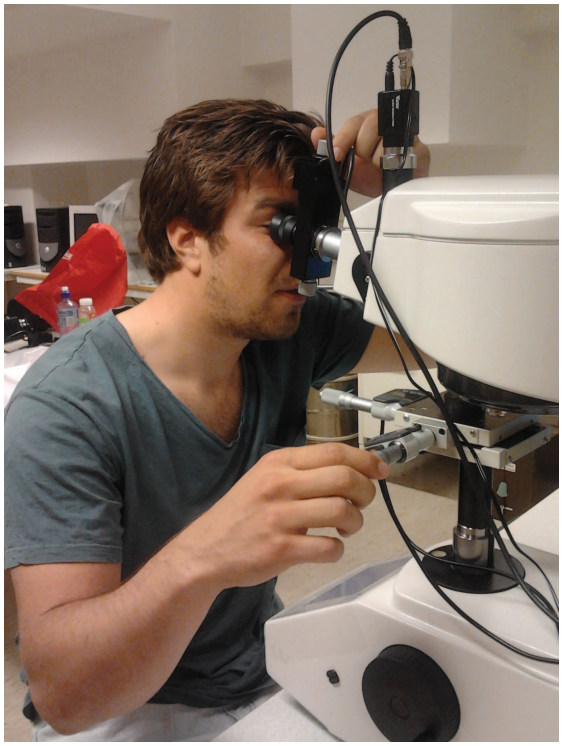

Figure 3.11: Vickers hardness testing with Mitutoyo HM-200

Figure 3.12: Location and numbering for Vickers hardness test points

Point nr.	**Location**	**Hardness nr.**	**Test type**	**Applied force** [kg]
1.	Bushing	118,8	HV	1
2.	Bushing	115,1	HV	1
3.	HAZ	149,3	HV	1
4.	HAZ	155,5	HV	1
5.	Weld	176,3	HV	1
6.	Weld	172,3	HV	1
7.	Disk	126,1	HV	1
8.	Disk	124,8	HV	1
9.	Shaft	211,9	HV	1
10.	Shaft	206,5	HV	1
11.	Sample rod	235,4	HV	1
12.	Sample rod	234,9	HV	1

Table 3.3: Results Vickers hardness test

The estimated ultimate tensile strengths of the materials from the different parts tested in the Vickers test is presented in table 3.4 on the next page. According to equation 2.10 on page 15, the Vickers hardness number is multiplied by $\frac{1}{0,3}$ to obtain an estimate for the ultimate tensile strength.

Material	**average HV**	σ_{UTS} [MPa]
Bushing	116,95	389,44
HAZ	152,40	507,49
Weld	174,30	580,42
Disk	125,45	417,75
Shaft	209,20	696,64
Sample rod	235,15	735,05

Table 3.4: Estimation of ultimate tensile strength

3.4 Finite Element Analysis

10 3D models were made in accordance with the technical drawings supplied by RHL (B on page 85). The results are used in the fatigue life assessments. The shaft is stepped in the drawings, but not in the models as these are not areas of focus. The models are named in table 3.5. In addition, two 2D sub models were made.

For 1 and 2 Pulleys
Without bushing
Without bushing w/cavity
Bushing
Bushing w/cavity
Broken bushing

Table 3.5: List of models made

The models without bushings were made to compare the fatigue life calculations with the existing data from RHL. This also gives a comparison of the stresses in the turbine, both with and without bushings. An analysis of the models with cavities at the weld for both with and without bushings is conducted. It is likely that the old turbines had such cavities since the welding procedure has not changed. Furthermore, two models simulating a case where the bushing has failed from fatigue are modelled. All cases were simulated for configurations of one and two pulleys.

3.4.1 3D Modelling

The area of interest is at the weld closest to the pulley, as this area have been subject to fatigue failure. In case the bushing would fail from fatigue, a simulation of this scenario is interesting with respect to redundancy. The 1 and 2 pulley broken bushing models are made to look into this issue. All models are made from 5 assembled parts.

Part: Shaft and Disk

For the 2 pulley models, symmetry in load and geometry was exploited the by making a half model. For the 2 pulley model without bushing, the disk is partitioned at the *hydraulic radius*, Γ, as shown in figure 3.13. This was done to later apply the resultant force of the flow. The interior of the model was also partitioned to facilitate application of hexahedral elements (as seen in figue 2.10 on page 23).

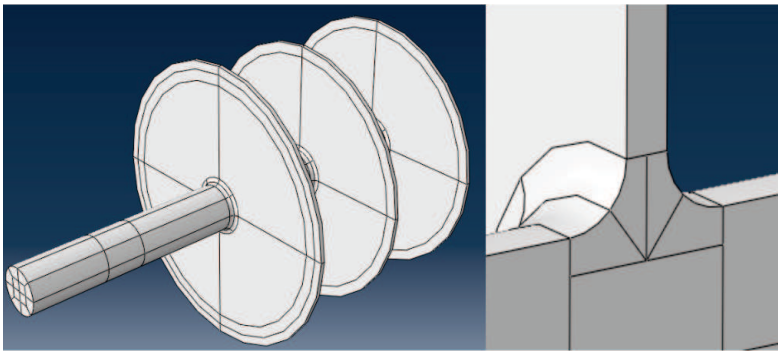

Figure 3.13: Shaft and disks with partition at blade radius on the left. On the right, partitions to facilitate application of quadrilateral elements inside the part at the disk root.

Part: Shaft with cavity

The part is made by introducing a cavity to the previous part. The approximate measurements of the cavity were taken from figure 3.14 and sketched onto the part. This area was seeded much more densely than the rest of the part to cope with the increased complexity of the geometry.

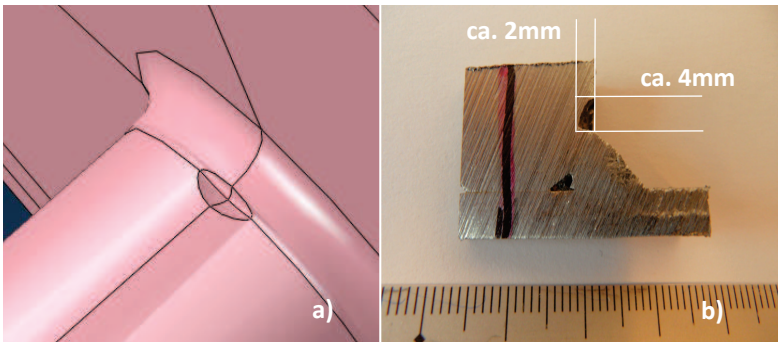

Figure 3.14: Cavity in model without bushing. Cavity geometry from b).

A cavity was introduced to Shaft and disk at the weld (figure 3.14a)), based on the measurements in figure 3.14b).

Part: Shaft for bushing

This part was made to facilitate the introduction of the bushing. It was made simply by removing the out-most disk on $Shaftanddisk$ and partitioning the shaft at the same point.

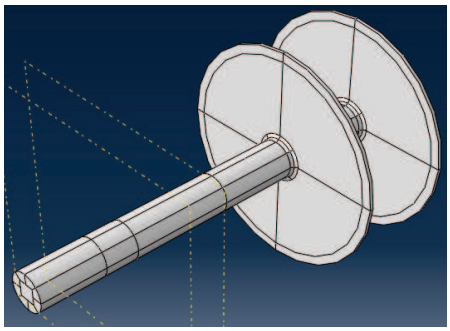

Figure 3.15: Shaft for bushing.

Parts: Disk with bushing, with and without cavity

The bushing and disk were made into one, solid part. The cavity was made as in Shaft with cavity. Presented in figure 3.16.

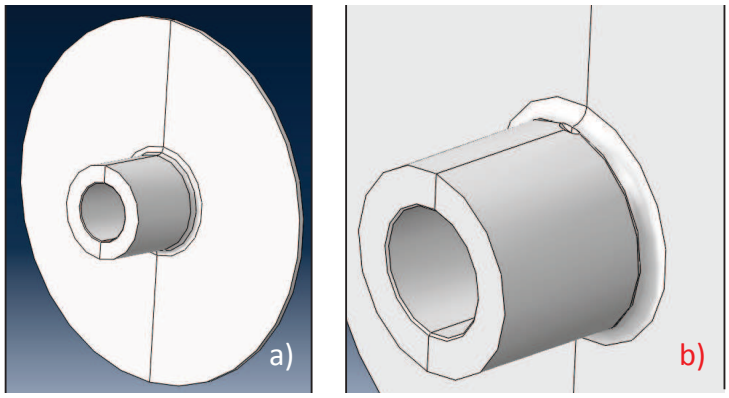

Figure 3.16: Disk with bushing, cavity on the right.

Assembly

In the 'Assembly' module of ABAQUS, the respective parts were positioned accordingly to complete the models. As an example, the 2 pulley bushing was made by assigning the 'Disk with bushing' to its correct position on 'Shaft for bushing' as seen in figure 3.17.

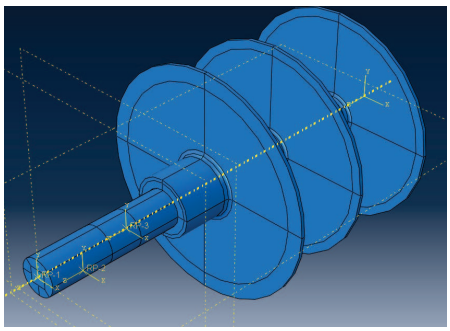

Figure 3.17: The assembly of the 2 pulley bushing model.

The 1 pulley models were assembled by adding the same parts to the assembly. As an example, the 1 pulley bushing model was assembled using the *Shaft for bushing* part twice. Then, the *Disk with bushing* part positioned on either side. The model is seen in figure 3.18.

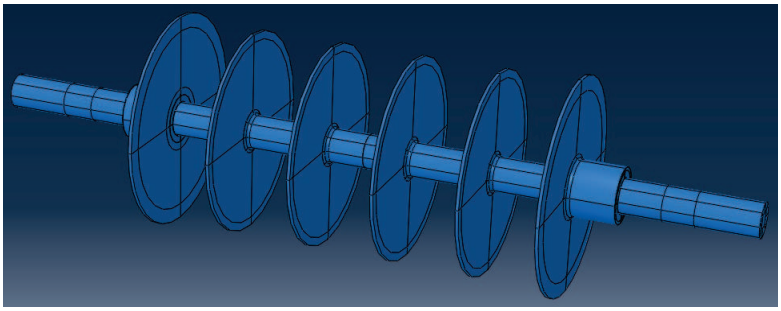

Figure 3.18: The assembly of the 1 pulley bushing model.

3.4.2 Constraints and boundary conditions

For the half model of the turbine with 2 pulleys, a symmetry condition is applied to the far end in the Z-direction. This boundary condition is called ZSYMM in ABAQUS and constrains the assigned area in the Z-direction and rotation around the X- and Y axis. To account for the exclusion of the turbine blades in the models, the outer edges of the disks were constrained in the Z-direction. This allows for the disks to deform appropriately. Both constrained areas are shown in figure 3.20.

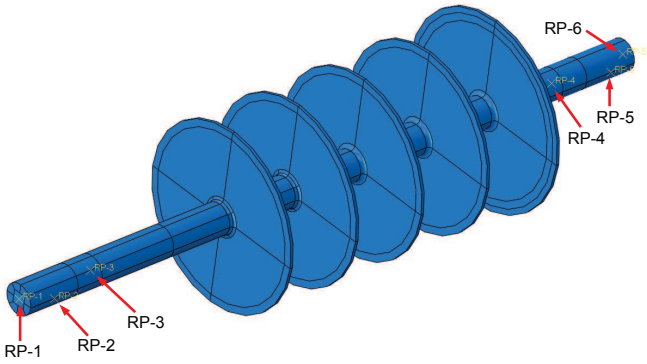

Figure 3.19: Overview of all RPs used.

In this section, references will be made to geometrical reference points (RPs). They are distributed on the model as shown in figure 3.19. The RPs 1, 2 and 3 are used in the 2 pulley models. RP-4 is used in the 1 pulley models in addition to the other RPs. The remaining are used in the 2 pulley broken bushing model, in addition to the previous.

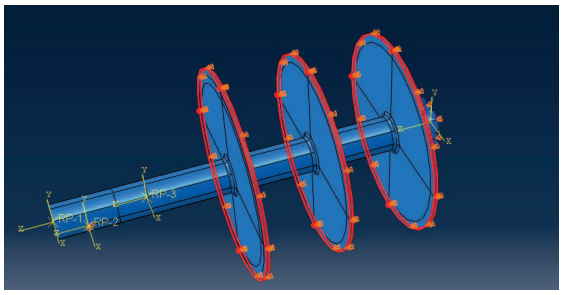

Figure 3.20: Highlighted areas are constrained in Z-direction. The area constrained with symmetry condition is the cross section surface at the far right end. 2 pulley model without bushing.

The bushing is constrained to the shaft using a tie constraint. The corresponding slave and master surfaces experience the same displacements and strains, therefore transferring forces between the parts. The constrained surfaces are shown in the figures 3.21 ans 3.22 below. The same constraint is used to tie the two shaft parts together in the middle of the 1 pulley models.

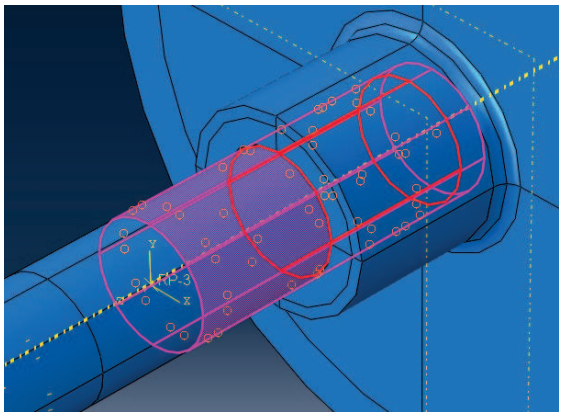

Figure 3.21: Red surface indicates the master surface, the pink is the slave surface.

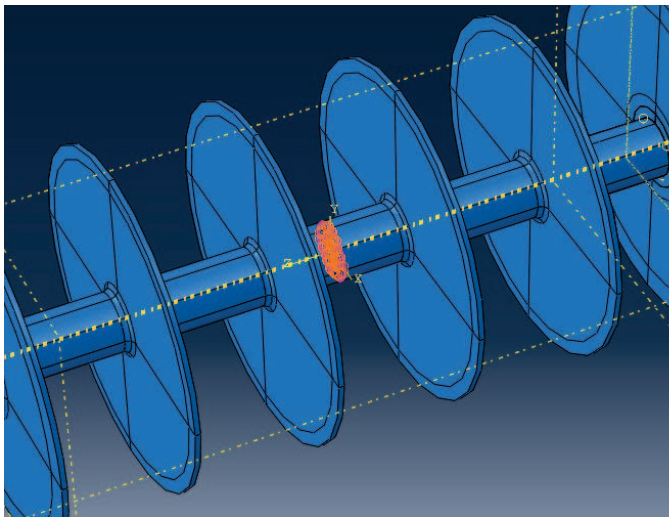

Figure 3.22: The two identical parts are tied where indicated to constrain the two parts together the 1 pulley models.

For the support of the model, *structural distributing coupling* constraints were applied to the centre of the positions bearings on the shaft surface. A partition had been made at the centre of the bearing to facilitate this. A reference point, RP-3, was created at the centre of the shaft at this partition. The surface edge of this partition was coupled to the reference point with respect to a coordinate system originating at RP-3. This is shown in figure 3.23. Subsequently, RP-3 was constrained in the X- and Y directions of the global coordinate system. For the 1 pulley models, the bearing at the far end was constrained in the same manner. In addition, the reference point for that bearing was constrained in the Z-direction as well for simple support.

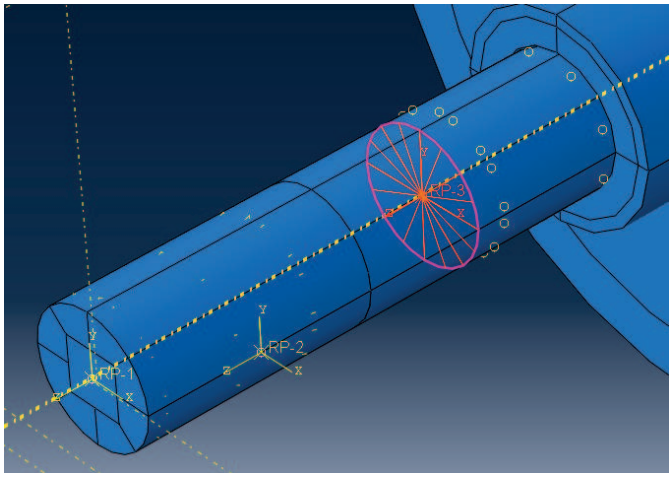

Figure 3.23: Constraint between reference point and edge. This simulates the behaviour of the turbine bearing.

The same type of coupling constraint was used for applying the *pulley force*. A partition had been made to define the surface for where the pulley force would act. A reference point, RP-2, was made on middle of 'the X side' of this surface, as seen in figure 3.24. The opposing side of the surface was constrained to RP-2 the same way as for the bearing (RP-3). This is also seen in figure 3.24.

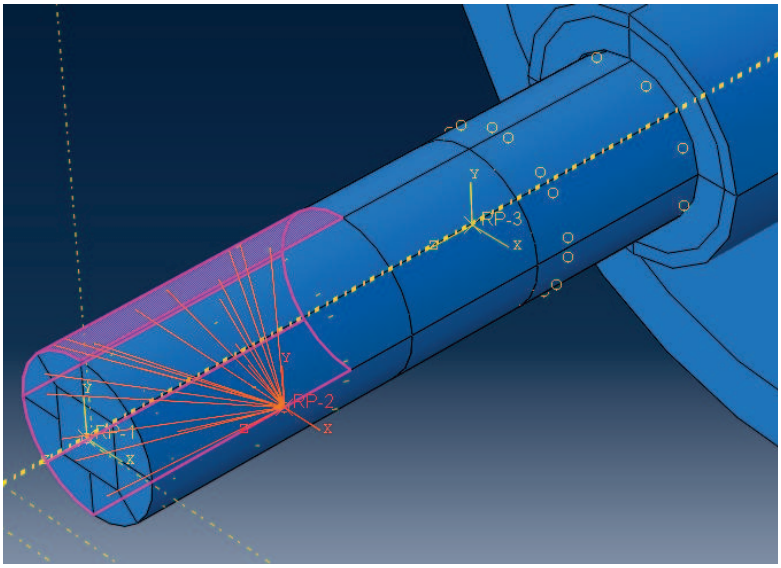

Figure 3.24: The pink surface was tied to RP-2.

Torsional equilibrium about the Z-axis was ensured by constricting the 'pulley surface' to RP-1, as seen in figure 3.25. The surface was coupled as with RP-2 and RP-3. RP-1 was subsequently constrained from rotating about the Z-axis, supplying the torsional equilibrium, yet allowing the pulley surface to deform from the resulting bending moment.

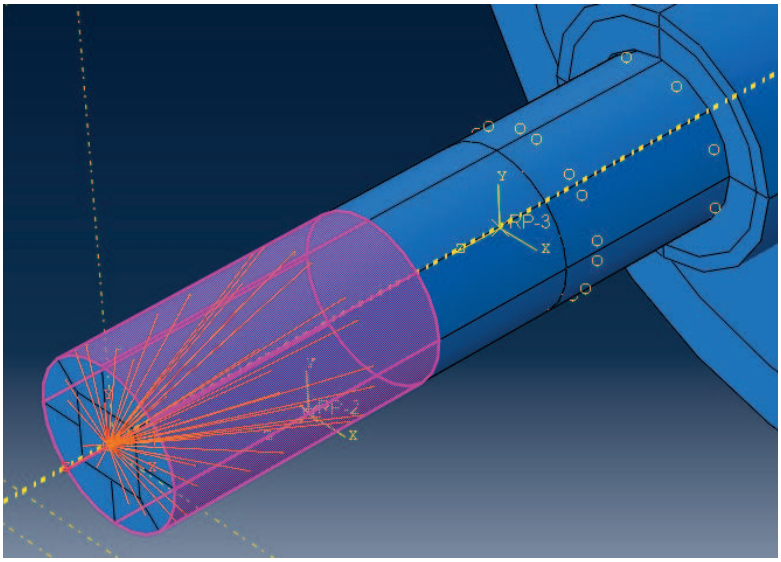

Figure 3.25: The indicated surface was coupled to RP-1.

3.4.3 Loads

The loads are applied to the models. The *flow forces* are applied to the disks at the hydraulic radius. Two point loads are applied to the centre disks, while one point load is applied to the out-most disks, where the attachment points of the blades are located. This reflects the real, physical load situation. The load scenario can be seen schematically in figure 3.27a) and in ABAQUS in 3.26b). This way of loading is somewhat conservative because of the shear stresses that occur in between the load and the shaft. This will be in addition to the shear stresses from the torsional moment it creates. This "additional" shear will not occur in 3.26b).

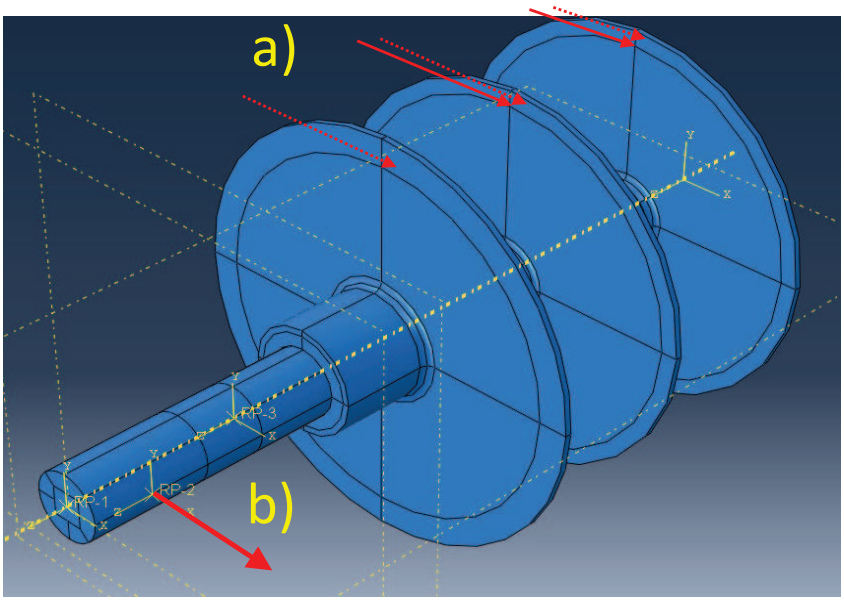

Figure 3.26: Taken from the 2 pulley bushing model. The flow forces are applied identically in the first 8 models in table 3.5.The dotted lines indicate point load on the opposite side of the disk. a) Flow forces. b) Pulley force applied at reference point, RP-2.

The *pulley force* is applied as a point load in the X-direction at RP-2 for all models. This is illustrated in figure 3.27 on the next page. For the 2 pulley broken bushing model the same load is applied at RP-6. The applied loads are listed in table 3.6 on the following page.

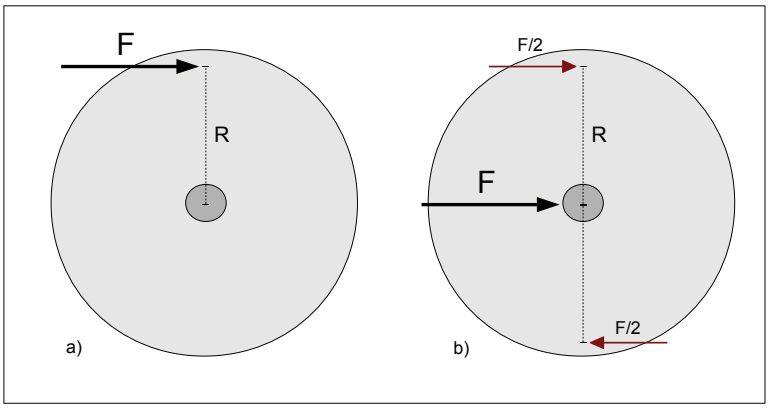

Figure 3.27: Two alternative load scenarios to introduce both torsional- and bending stresses. R indicates the blade radius.

Point loads	*1 pulley*	*2 pulleys*
Flow force at 50 m head (a)	582 N	1080 N
Pulley force (b)	7800 N	7280 N
$Flow force at 7 m head (a)	N/A	404 N)

Table 3.6: The pointloads used for the analyses

For the broken bushing models, the flow forces are applied as in the other models, except the point of the shaft where the out-most disk was removed. Here, the loads are applied as illustrated in figure 3.27b).

3.4.4 Meshing

All models are meshed with linear 3D elements. The element types assigned to the parts are

8 node hexahedral elements - Shaft with disk, Shaft for bushing and Disk with bushing

4 node tetrahedral elements - Shaft with cavity and Disk with bushing and cavity

Both element types are explained in section 2.6.1 on page 21.

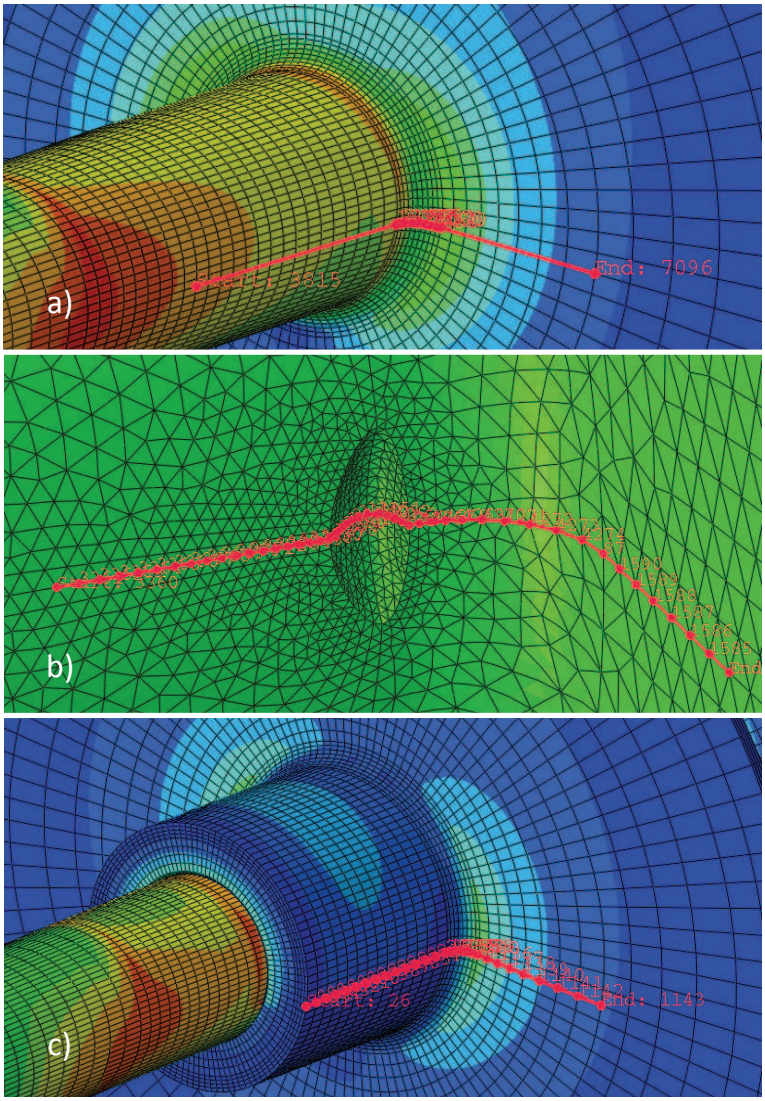

Figure 3.28: All stresses were extracted along the paths, starting from the left. a) Old turbine. b) Cavity. c) Bushing.

3.4.5 2D models

Two 2D models were made to assess the potential consequences, in case of a cavity in the disk. This was done to observe the difference in stress at both sides of the weld, with and without cavities. Both analyses were run and stress were extracted from both sides of the weld in both cases. Both models were loaded with a unit load.

Chapter 4

Results

4.1 Results flow analysis

A numerical analysis is conducted in a spreadsheet E.2 and Matlab E.1 with the maximum flow for turbine of subject. The maximum force acting on one blade is used to scale the torque distribution on each blade using the strain gauge curve found in Walseth [2].

The tested turbine, Hindu Kush, is designed for maximum net head of 50 meter ($H_e = \ 50m$) at a volume flow of 325 liter/s ($Q = 0,325m^3/s$) for a HKT with two pulleys. The maximum flow rate when the turbine is connected to one pulley is 175 liters/s ($Q = 0,175m^3/s$). Theses values is used throughout the flow calculation as it gives the biggest forces on the turbine.

4.1.1 Forces on turbine blades

The amount of torque contributed by one blade is found from equation 2.5 on page 11 from section 2.2. The value is found to be $T_c = 30,5Nm$. The force acting on blade is found by using equation 2.6. The hydraulic arm, Γ, from equation 2.7 is $147,65mm$. The geometric values for the rotor and governing equations are processed in a spreadsheet. With the maximum

design value for net head, the maximum resultant force on one blade is $F = 207N$ for 2 pulley model.

Torque distribution on individual blades

To quantify where torque is transferred in the runner, the torque distribution are scaled after figure 2.4 from section 2.2.1. The scaling is done by using the amount of torque by each channel T_c as the first peak from figure 2.4 and the same relation between the first valley and second peak as in figure 2.4. The last blade is set to contribute with no torque, as it is empty. To match the total torque from the runner calculated with the overall efficiency (η), and available net head (H_e), the peaks are adjusted. The first peak is adjusted up iterative by a loop, and the first valley and second peak is scaled by the first peak. The script performing this iteration is presented in Appendix E.1.

$$\begin{aligned} T_s &= \frac{\eta \rho g Q H_e}{\omega} \\ &= \frac{0{,}786 \cdot 998 kg/m^3 \cdot 9{,}81 m/s^2 \cdot 0{,}325 m^3/s \cdot 50m}{87{,}12 rad/s} \\ &= 1438 Nm \end{aligned} \tag{4.1}$$

Figure 4.1 gives an idea of how much torque each blade channel contributes to the overall torque transfer. With the runner rotating, the blade number notation is a snapshot of the system, shown in figure 4.2. As seen in figure 4.1, the first peak is at blade number 7, and the second peak is reached at blade 14. The amount of torque per blade is the torque contributed by the five channels that over-span each blade seen in figure 1.3 on page 4.

Torque transfer and efficiency

The overall torque transfer is calculated based on the equations presented in section 2.2.2 and appendix C.

To validate the results, the efficiency based on the torque transfer equations is calculated and compared to the measured efficiency from Walseth [2].

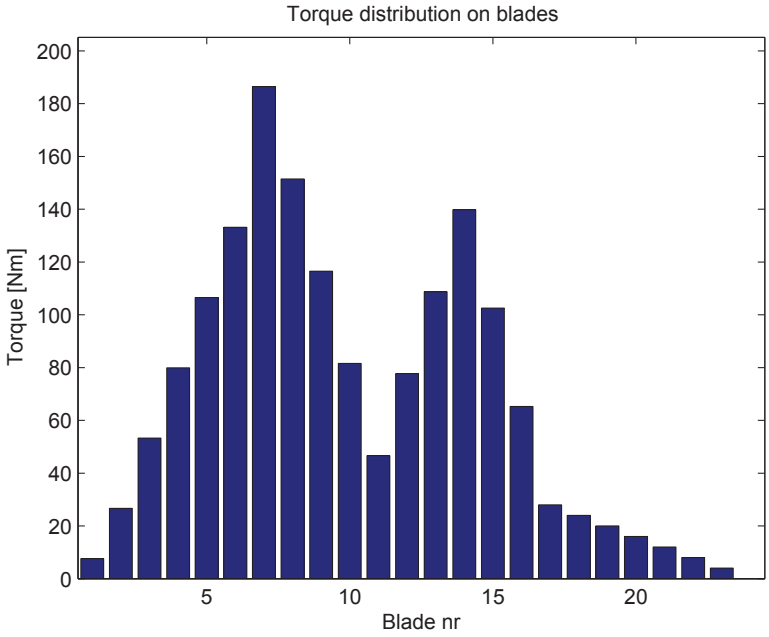

Figure 4.1: Torque on blades

Two pulleys

Results with two pulleys, $H_e = 50m$, $Q = 0,325m^3/s$;

From the first stage of the cross-flow, the calculated torque from one blade channel from equation 2.5 is shown in equation 4.2.

$$\begin{aligned} &T_{c1} = Q_c\rho(c_1 R_o cos\alpha_1 - u_2 R_i) \\ &= 0,0082 \cdot 1000 \cdot (29,71 \cdot 0,17 \cdot \cos(16°) - 14,28 \cdot 0,1168) \\ &= 30,5Nm \end{aligned} \tag{4.2}$$

The result of the torque contribution from the second stage of the cross-flow is shown in equation 4.3.

$T_{c2} = Q_c\rho\, u_3 R_i$

$$T_{c2} = 0,0082 \cdot 1000 \cdot 9,81 \cdot 0,1168 = 9,39Nm \tag{4.3}$$

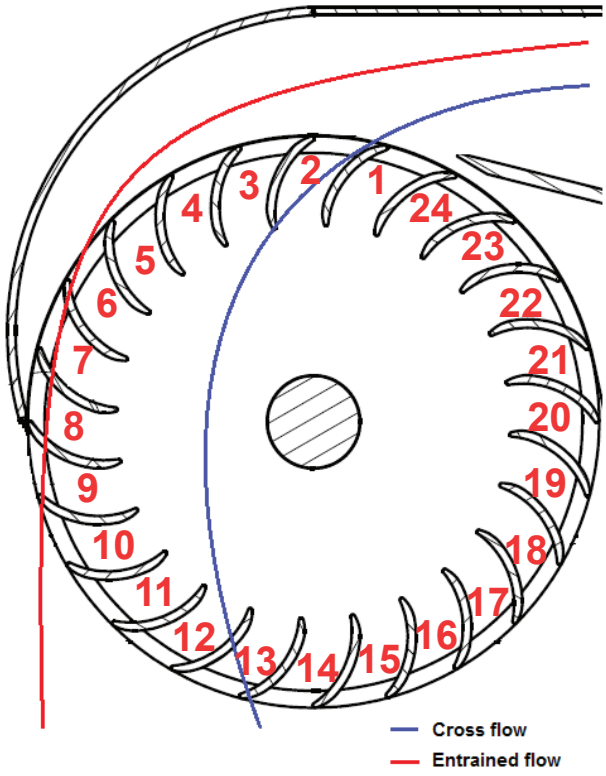

Figure 4.2: Snapshot of rotating runner with blade numbers

The second stage of the cross-flow contributes with 76,5% of the torque transfer, while the second stage contributes with 23,5%.

This gives an overall torque transfer to the shaft as in equation 4.4. The constant n is the number of blades contributing in stage 1 and stage 2 of the torque transfer. The number is chosen to be 8, based on the geometry in figure 4.2. The constant s is the number of blade spans in the rotor, which is 5.

$T_s = n \cdot s(T_{c1} + T_{c2})$

$$T_s = 8 \cdot 5\,(30,5Nm + 9,39Nm) = 1595,5Nm \tag{4.4}$$

Reviewed for equation 2.2 $\eta = \frac{T_s \omega}{\rho g Q H_e}$ and for this case with the angular velocity of the turbine ω= 87,12 rad/s calculated from equation 2.4, the

theoretical efficiency obtained using this conservative method, with respect to forces on turbine, is shown in equation 4.5.

$$\eta = \frac{1595 \cdot 87,12}{1000 \cdot 9,81 \cdot 0,325 \cdot 50} = 0,872 \tag{4.5}$$

This gives a shaft power of 139 kilowatts [kW].

One pulley

Results with one pulley, $H_e = 50m$, $Q = 0,175m^3/s$;

The same calculations as with two pulleys is done with the turbine connected to one pulley. The only difference is the maximum allowed flow rate, the geometry is the same. Following is the calculation of total shaft torque T_s, and efficiency. The overall shaft torque for 1 pulley turbine follows in equation 4.6.

$$T_s = n \cdot s(T_{c1} + T_{c2}) = 8 \cdot 5\,(16,4Nm + 5,1Nm) = 859,1Nm \tag{4.6}$$

The hand-calculated efficiency of the 1 pulley turbine follows in equation 4.7.

$$\eta = \frac{859,1 \cdot 87,12}{1000 \cdot 9,81 \cdot 0,175 \cdot 50} = 0,872 \tag{4.7}$$

This gives a shaft power of 75 kilowatts [kW].

4.2 Analytical shaft stress calculations

The calculations done in this section are based on the theory and equations presented in section 2.4 on page 15. Firstly, the bending of the shaft due to forces from pulley and rotor is calculated. As mentioned, the point of interests is the point x from figure 2.6. Then the contribution from the shaft torque is accounted for as torsion. The bending moment and torsion in the shaft results in axial stresses and shear stress, which are described in section 2.4.

4.2.1 Torsion and bending moment

Torsion is a result of twisting of the shaft due to applied torque.

Bending moment

The two driving forces causing bending moment in the shaft is the pulley force and the distributed load from the blades. Their contributions to the total bending moment are calculated separately and then super positioned. The upper side of the shaft is defined to be in tension.

The contribution from the pulley forces is calculated from equation 2.11 in the case with one pulley. The contribution from the distributed force W, shown in equation 2.12, and acts in the opposite direction of the bending moment from the pulley force.

The pulley force F is given by A. Austegard [13] and is based on measurements and common practice in the Afghan villages. With one pulley connected to the shaft, the force F is given to be 7800 N, and 7280 N in each pulley when connected to two pulleys.

The distributed load W is based on an assumption done by A. Austegard [13] that six of the blades in the runner contributes with force which cause bending of the shaft. The force acting on one blade with the maximum flow ($Q = 0,175 m^3/s$) assigned for the turbine with one pulley is

111 N. With five channels per blade, and 6 blades contributing with bending. Given the width of the rotor of 0,650 m, the distributed force W is 5123 N/m. When the turbine is equipped with two pulleys, the maximum allowed flow rate is $Q = 0,325m^3/s$. This gives a force on each blade channel of 206 N, which results in a distributed load of 9508 N/m.

The total bending moment in point x from figure 2.6 on page 16 are shown in equation 4.8. The equation is based on classic beam theory and the dimensions from the 1 pulley Hindu Kush turbine, showed in Appendix B.

$$\begin{aligned} M_b &= \frac{Fc(a+b)}{l} - \frac{Wba}{2} \\ &= \frac{7800N \cdot 0{,}0955m(0{,}136+0{,}65)m}{0{,}922m} - \frac{5123N/m \cdot 0{,}65m \cdot 0{,}136m}{2} \\ &= 408,6Nm \end{aligned} \tag{4.8}$$

With to pulleys and the corresponding forces, the numerical values for the bending moment is shown in equation 4.9.

$$\begin{aligned} M_b &= \frac{Fc(2a+b)}{l} - \frac{Wba}{2} \\ &= \frac{7280N \cdot 0{,}0955m(2 \cdot 0{,}136+0{,}65)m}{0{,}922m} - \frac{9508N/m \cdot 0{,}65m \cdot 0{,}136m}{2} \\ &= 275Nm \end{aligned} \tag{4.9}$$

4.2.2 Shaft stresses

Bending moment and torsion resulting in a biaxial stress situation in the shaft.

Axial and shear stresses

The upper side of the shaft from figure 2.6 is in tension. Axial stress on the outer surface at point x from the same figure is given by equation 2.15. The numerical values for bending moment and geometry are inserted in the mentioned equation and presented in table 4.1.

The shear stress at the weld toe on the shaft at point x from figure 2.6 on page 16 is calculated from equation 2.16 by inserting the numerical values for torsion and geometry of the shaft. The results are presented in table 4.1.

	Tension σ[MPa]	**Shear τ[MPa]**
1 pulley	25,01	26,33
1 pulley with bushing	6,11	6,43
2 pulleys	16,84	24,41
2 pulleys with bushing	4,11	5,96

Table 4.1: Hand-calculated axial- and shear stresses in HKT at weld toe

4.3 Results from FEA

4.3.1 3D models

For all the models, the Von Mises stresses in MPa were extracted to be used in the fatigue life evaluations. The stresses were extracted by means of a *path* in ABAQUS (figure 3.28 on page 50) A path is a list of nodes that allows plotting whatever wanted node value against the distance covered by the path. The results are graphically presented with five plots. All plots show *distance along path* versus *Von Mises stresses*. The paths are shown in 3.28 on page 50. All paths start at the same distance from the weld toe for easier graphical comparison of the results.

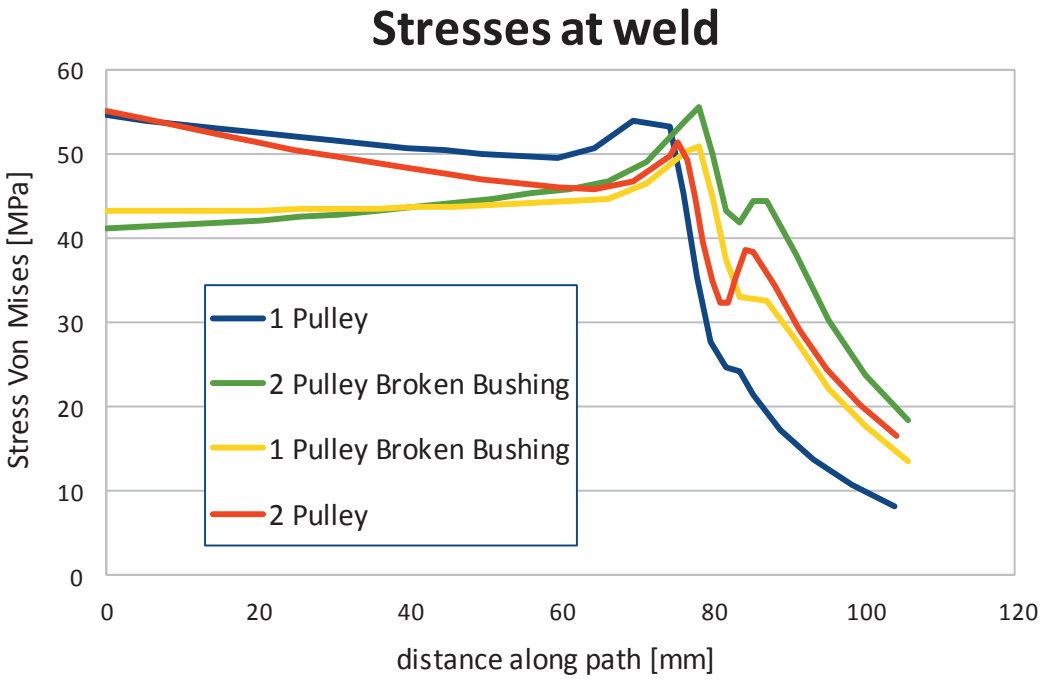

Figure 4.3: Von Mises stress in the original turbine without bushing at weld. Comparison of one and two pulley configurations, with and without broken bushing.

The stresses in the weld of the four different configurations are quite similar, as seen in figure 4.3. The slight peak at approximately 75 mm (figure 3.28b)along the path is at weld toe on the shaft side. The stresses in the weld of the out-most disk where the bushing has failed, do not differ greatly from the outer disk on original turbine without bushing.

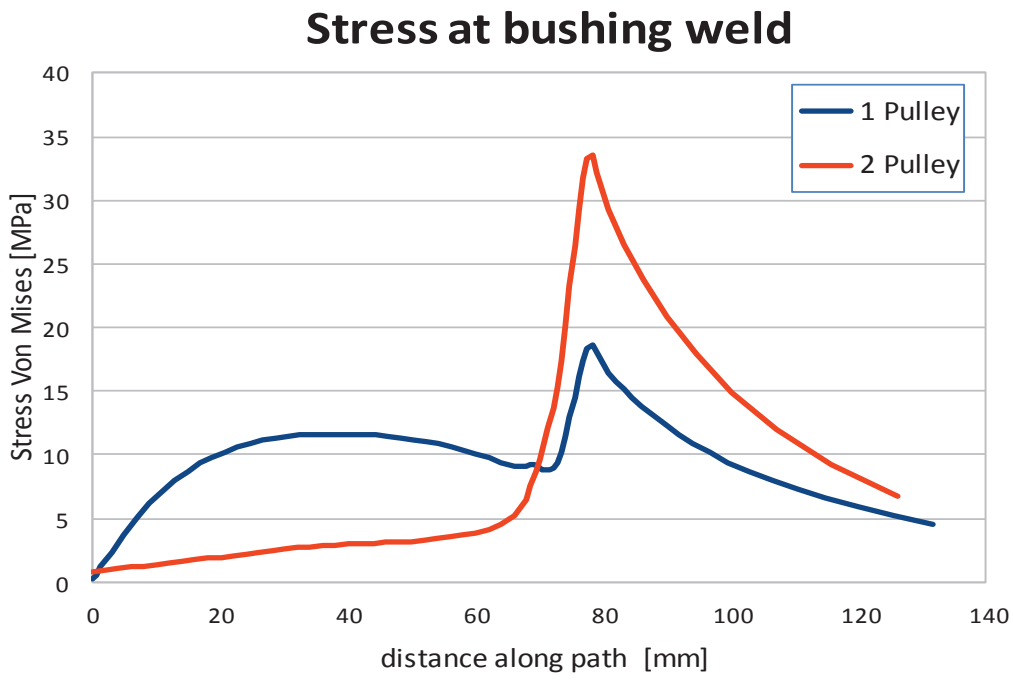

Figure 4.4: Comparison of stresses of one and two pulley configurations of shaft with bushing.

Figure 4.4 shows that the stresses for the one and two pulley configurations differ significantly. The nominal bushing stresses differ significantly, but remain under 12 MPa, which is lower compared to the shaft stresses in figure 4.3. However, ats the weld at around 80 mm along the path in figure 3.28c, we can see a doubling of stress in the 2 pulley configuration. The highest stresses, approximately 33 MPa, have also moved to the other side of the weld and on to the disk, in comparison with the weld on the original turbine without bushing.

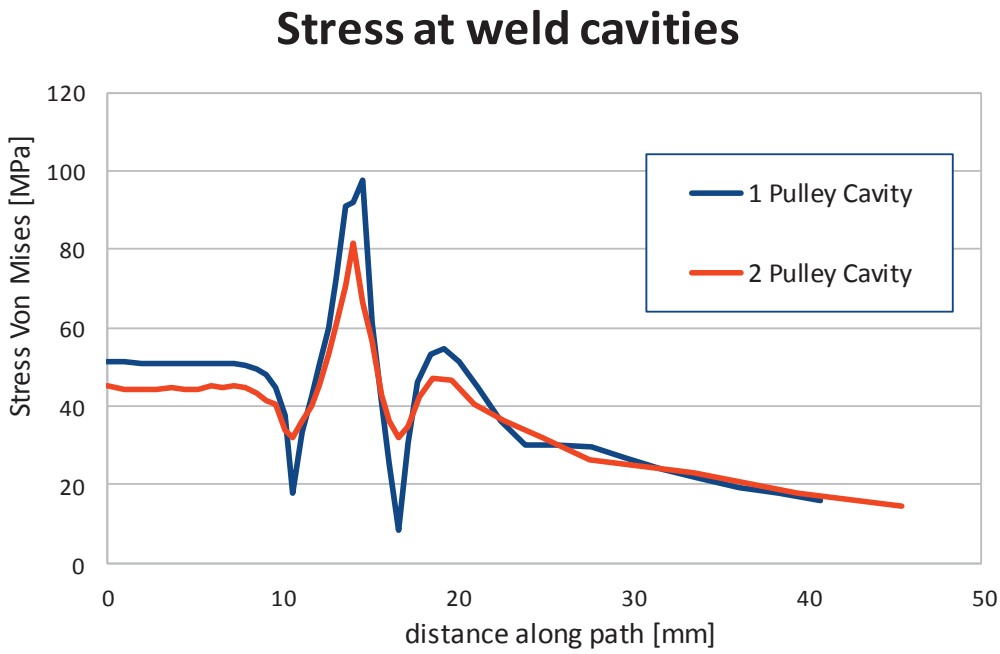

Figure 4.5: Comparison of stresses of original turbine without bushing with cavity at weld for one and two pulley configuration

Figure 4.5 shows the stress concentrations at the cavity for both pulley configurations without bushings. The stress decreases at the cavity mouth at approximately 10 and 16 mm along the path with reference to figure 3.28 on page 50b. The SCF is at approximately 2 for both configurations, however slightly higher for the one pulley configuration. This figure shows, by far, the highest stresses in all the analyses performed.

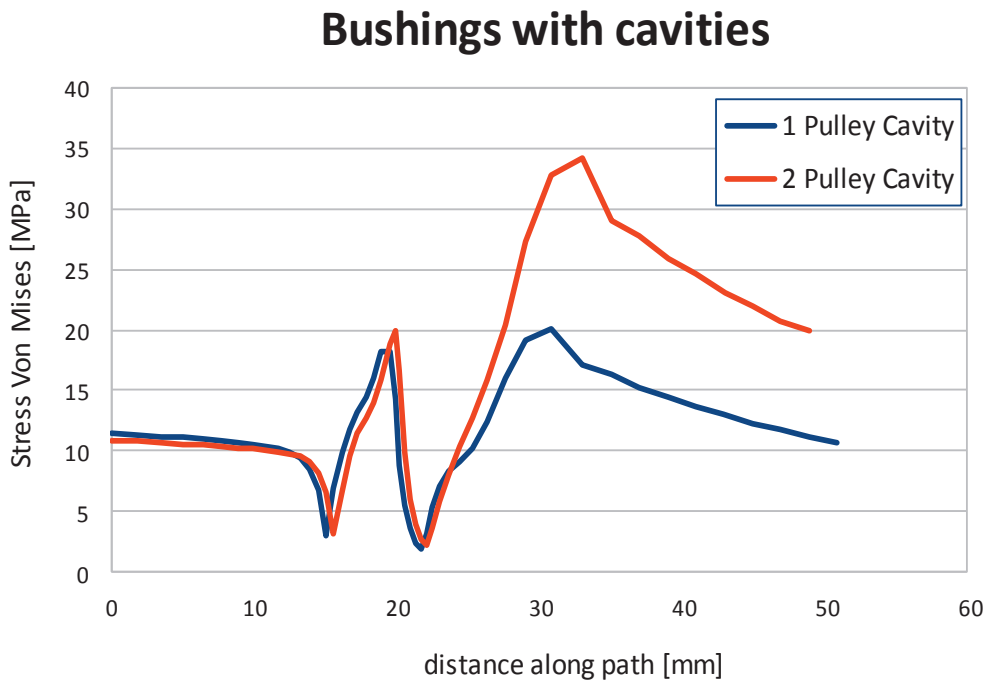

Figure 4.6: Comparison of stresses of one and two pulley configurations of shaft with bushing.

The stresses at the bushing weld are nearly identical, even at the cavity, as seen in figure 4.6. At about 30 mm along the path in figure 3.28b, the stresses are nearly doubled in the two pulley configuration. This is at the root of the disk, very similar to the stresses at the same spot in figure 4.4.

The relative improvement of introducing a bushing on the shaft follows from table 4.2. The stress reduction is the percentage decrease in Von Mises stress at the weld toe with introduction of bushing.

	Without bushing	With bushing	Stress reduction
1 pulley	55,2 MPa	15,0 MPa	72,8%
1 pulley cavity	97,6 MPa	18,2 MPa	81,4%
2 pulleys	55,2 MPa	26,2 MPa	52,5%
2 pulleys cavity	81,3 MPa	20,1 MPa	75,3%

Table 4.2: Relative improvement with introducing of bushing

4.3.2 2D models

Stresses were extracted from both sides of the weld for both 2D models. The stress distributions are illustrated in figures 4.7 and 4.8, respectively cavity in bushing and cavity in disk.

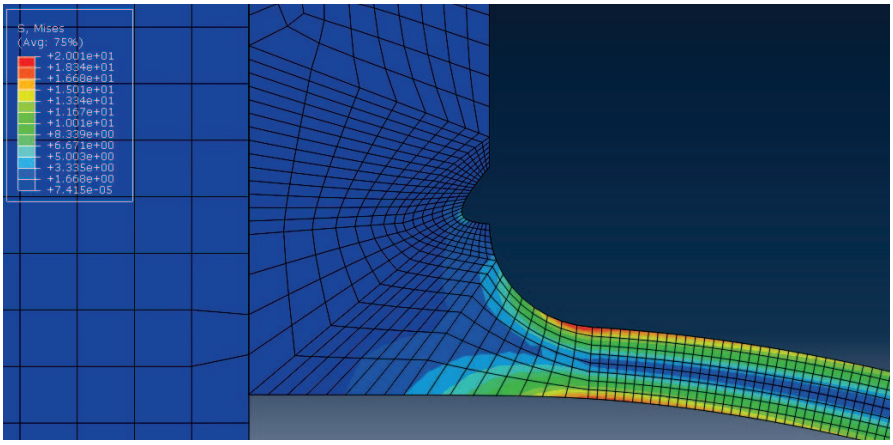

Figure 4.7: Stress distribution for 2D model with bushing cavity.

Side og weld	No cavity	Cavity
Bushing	2,7 MPa	5,9 MPa
Disk	20 MPa	73 MPa

Table 4.3: Nominal- and cavity stresses for the 2D models.

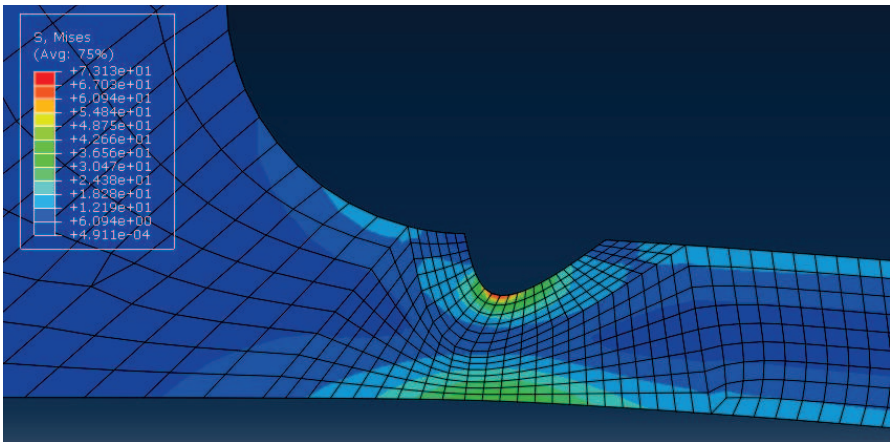

Figure 4.8: Stress distribution for 2D model with disk cavity.

The results are presented in table 4.3.

7 meters head

The following results are from analysis with 7 meters net head. This analysis is done to find the stress level of the turbine that have been subject to fatigue fracture. The analysis is done with the 2 pulley model without bushing.

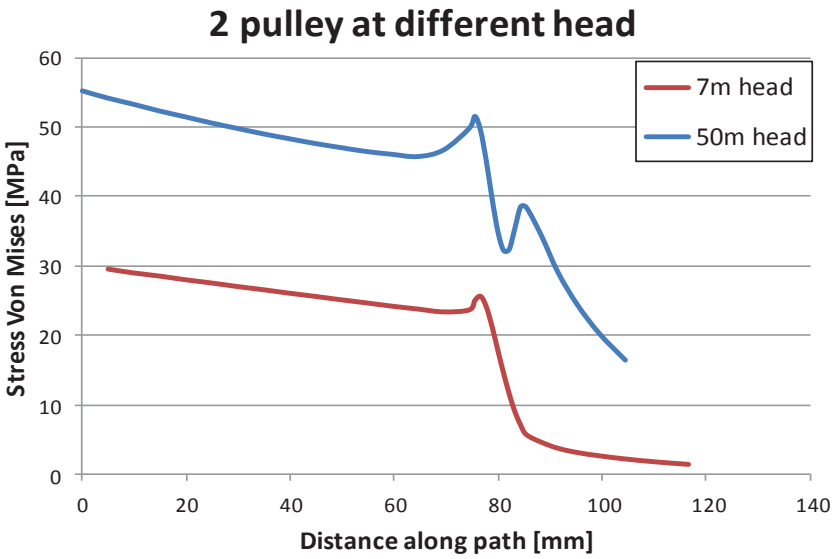

Figure 4.9: Stresses at path for 2 pulley without bushing at 7 meters and 50 meters net head

Figure 4.9 shows substantially lower stress level for the turbine with load caused by 7 meter net head. The Von Mises stress obtained at the weld toe is 25 MPa.

4.4 Fatigue life

Following is the fatigue life for the shaft both with and without bushing. The calculations are done with maximum head (50m) and a flow of $0,175m^3/s$ for the case with one pulley, and $0,325m^3/s$ for the turbine with two pulleys. The rotational speed of the shaft is 832 rpm, hence the duration of one load cycle is 0,0722 seconds.

With the use of the modified version of Basquin's equation (2.21), a conservative value of the number of cycles before failure is calculated for both the original shaft and shaft with bushing.

This gives an expression for both the shaft with and without bushing rewritten in order to find the number of cycles to failure, shown in equation 4.10.

$$N = \frac{1}{2}(\frac{\sigma_{a,e}}{R_m - \sigma_{m,e}})^{\frac{1}{b}} \tag{4.10}$$

The parameter $R_m^{'}$, which is the cyclic tensile strength is assumed to be close to the ultimate tensile strength [8, pg. 12] (σ_{UTS}) for the material. By this assumption, the values for σ_{UTS} from table 3.4 on page 38. The found tensile strength for the shaft material is close to 700MPa, which will be used. The bushing is made of another material with measured tensile strength of 390MPa.

4.4.1 Determine slope number b for S-N curve

Basquin's equation depends on the correct value for the slope parameter b from equation 2.20 on page 21 to make any sense when calculating fatigue life. The turbine without bushing has been subject to fracture after one year of service. According to RHL, the turbine has been running 5 hours a day with an average of 7 m head. 7 m head gives a rotational speed of 311 rpm according to equation 2.4 on page 10 and translated into revolutions per minute, with one load cycle per revolution. This gives a fatigue life for the broken shaft of N = 34054500 cycles. Rewriting Basquins' equation

with respect to b gives equation 4.11. The input for the R_m is Ultimate Tensile strength found for the shaft material of 700 MPA. For the stress amplitide, the value found in section 4.3.2 on page 65 for the 7 m head turbine is 25 MPa.

$$b = \frac{log(\frac{\sigma_a}{R_m})}{log(2N)} = \frac{log(\frac{25MPa}{700MPa})}{log(2 \cdot 34054500)} = -0,183 \tag{4.11}$$

The S-N curve slope parameter b is found to be -0,183 based on equation 4.11.

Figure 4.10 shows the S-N curve for the shaft and bushing material, based on Basquin's equation with b=-0,183.

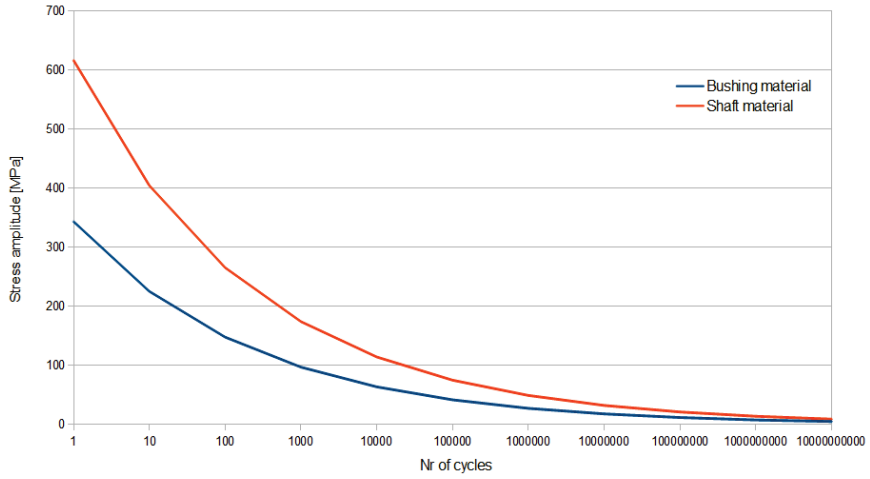

Figure 4.10: S-N curve for shaft and bushing material

Figure 4.10 shows that the shaft material has higher fatigue limit at any number cycle than the bushing. material. This is shown with the curve for the shaft material is above the curve for the bushing material.

Figure 4.11 shows the S-N curves for the shaft material for different values of the slope parameter b.

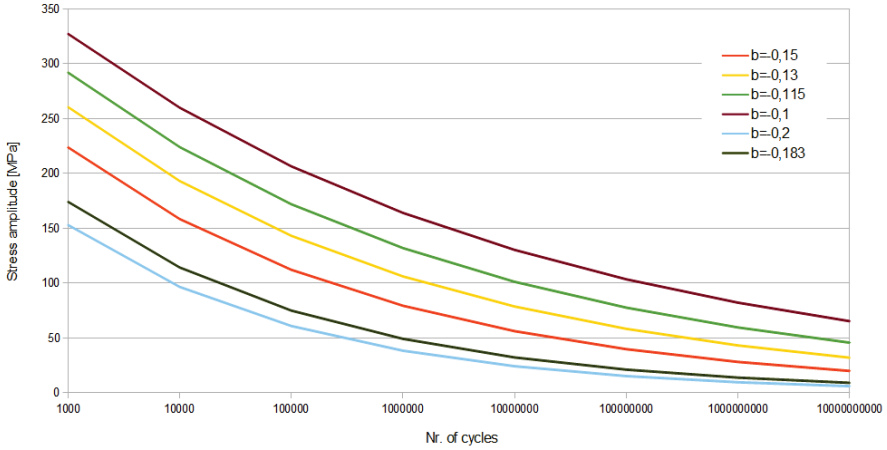

Figure 4.11: Comparison of S-N curve for bushing material for different values for slope parameter b

Figure 4.11 shows that the fatigue limit varies with different values for slope parameter b. The lower slope parameter, the higher fatigue limit.

4.4.2 Hand calculations

Based on the theory from section 2.5 on page 20, and hand-calculated stress levels found in section 4.2.2, the fatigue life of the shaft is estimated.

Stress amplitude and mean stress

As mentioned in section 2.4.3 on page 18, oscillations in the torque output adds to the equivalent stress amplitude. The average calculated torque output has to be equal the output corresponding to the efficiency found by Walseth [2] of 78%. An upper limit was set to be when 8 blades contributing with torque transfer. The lower limit is when 6,4 blades contributing to the total torque transfer. This difference gives a small amplitude for the shear stress (τ_a) which are included in the equivalent stress amplitude.

The stress amplitude is equivalent von Mises stress from equation 2.17 on page 18. The bending moments contribution to the stress amplitude, $\sigma_{a,e}$

are equal the maximum tension stress from table 4.1 on page 59.

According to Sines equation (2.18 on page 19) i the contribution from the mean stresses to the fatigue life zero. As only torsion contributes to the equivalent mean stress, the minimum value of Sines' rule will be $\sigma_{m,e} = \sigma_{xm} + \sigma_{ym} = 0$.

Stress consentration factor (SCF) is an important parameter when calculating the stress at the weld toe (σ_c). The only way of getting the correct SCF for a complex loading situation and geometry is through testing and FEA. Based on geometry and stress situation, a fair approximation of SCF=1,8 is made based on Roark's formulas for stresses and strains [14, tab 17.1].

The results are presented in table 4.4. The results are with maximum load, and the turbine running 24 hours a day.

Pulleys	Bushing	R_m [MPa]	$\sigma_{a,e}$ [MPa]	SCF	σ_c [MPa]	N (cycles)	Fatigue life
1	No	700	25,42	1,8	45,76	1487535	1,5 days
1	Yes	390	6,21	1,8	11,18	3289941888	7 years
2	No	700	17,34	1,8	31,21	12029900	10 days
2	Yes	390	4,23	1,8	7,61	26816194648	61 years

Table 4.4: Presentation of hand-calculated fatigue life based on Basquin's equation with b=-0,183

4.4.3 FEA

The stress levels found in the Finite Element analysis are studied further to give a better input in the fatigue analysis. Table 4.5 on the following page presents the results for the turbine running non stop 24 hours a day with maximum load of 50 meters head and 832 rpm.

Test nr.	Pulleys	Bushing	Cavity	R_m [MPa]	$\sigma_{a,e}$ [MPa]	N (cycles)	Fatigue life
1.	1	No	No	700	55,18	534590	0,5 days
2.	1	No	Yes	700	97,63	23654	30 minutes
3.	1	Yes	No	390	15,00	26981419	23 days
4.	1	Yes	Yes	390	20,07	5496013	5 days
5.	2	No	No	700	55,19	534061	0,5 days
6.	2	No	Yes	700	81,32	64226	1,3 hours
7.	2	Yes	No	390	26,24	1270258	1 day
8.	2	Yes	Yes	390	34,27	295314	7 hours

Table 4.5: Presentation of fatigue life based on stress levels from FEA with slope value $b = -0,183$

In table 4.6 follows the results for fatigue life for the same parameter as in table 4.5 except the slope steepnes parameter b is changed to -0,13. Calculations were carried out with $b = -0,13$ for comparative reasons.

Test nr.	b	N (cycles)	Fatigue life
1.	-0,13	153468342	128 days
2.	-0,13	1904814	1,5 days
3.	-0,13	38316018417	87 years
4.	-0,13	4079820344	9 years
5.	-0,13	153254570	127 days
6.	-0,13	7771656	6,5 days
7.	-0,13	518955145	433 days
8.	-0,13	66558670	56 days

Table 4.6: Presentation of fatigue life based on stress levels from FEA and slope value b=-0,13

Chapter 5

Discussion and conclusions

5.1 Discussion

5.1.1 Metallurgy

The difference in grain size between figure 3.6 on page 32 and 3.7 would render differences in ductile behaviour. Smaller grain sizes makes the material more ductile [12]. RHL informed us initially that the test rod and the shaft of the sample would be of the same material. This seems less likely after considering the difference in grain size. The two materials would have different stress-strain curves.

The low pearlite content in the bushing would decrease the yield strength of the material. This might also reduce the crack initiation time for the material, making it more prone to fatigue failure.

There is a high density of inclusions in the materials. If such inclusions are near the surface, they may become initiation points for crack propagation, hence potentially shortening the components fatigue life.

The micro crack we found are not in an area with large stresses. If they were, the fatigue life would de drastically reduced. However, if these kinds of cracks were to occur close to a surface, they would most likely start to

propagate. It is suspected that there might be more cracks around the weld, making it likely that the component would fail from fatigue.

5.1.2 Vickers hardness test

The Vickers test was done with a micro Vickers hardness test machine. Ideally, the test should have been done with a machine able to apply higher loads on a bigger area. This for excluding the effect of small variations in the micro structure. On the other hand, the test was conducted to give an estimation of the tensile strength of the material. The relationship between Vickers hardness, yield strength and tensile strength are not carved in stone, but have been proved to fit well for most materials. Because of low consistency of which materials is used to fabricate the turbine, an exact value is not needed. The hardness values differs much, from 117HV1 on the bushing material, to 209HV1 for the material used in the shaft. It is comforting that the best suited material available is used in the shaft.

5.1.3 Flow analysis

The result for the shaft torque is conservative as expected. It is calculated to be 1596 Nm, while 1438 Nm is the torque obtained with the highest measured efficiency for the turbine with two pulleys at maximum load. With the assumption of no loss and all of the entering water follows the cross-flow pattern, it is not too far off. In addition The calculated maximum torque is meant for finding the cyclic torque by using the measured efficiency as the average value. The same is for the turbine with one pulley.

When it comes to the result for torque contribution done by each blade, or more precisely where in the turbine the torque transfer is done, the figure 4.1 on page 54 does not tell the whole truth. The diagram is scaled to match the overall torque transfer, but it is expected that at some point the torque contribution will be negative. When the blades are empty, no energy can be extracted from the water, which means blades 17 - 24 illustrated in figure 4.2 on page 55 should have a negative effect on the overall shaft torque. The obstacle was to match the highest peak with the

calculated maximum force acting on one blade and the graph showing the response for one rotating blade.

5.1.4 Shaft stress

The idea behind estimating the stresses at the weld toe is to have an impression of what to expect from the FE analysis. Assuming the shaft to act like a simple beam without including the increased stiffness of the turbine blades is for simplicity reasons. The values obtained are on the other hand quite feasible. The stress is reduced with introducing of bushing is 75,6 %. It is expected that the bushing will have a positive effect on the stress distribution, but not that much. In the real situation, the stress distribution will be far more complicated.

5.1.5 FEA

Alternatively, the loads could be applied to the disks in the following way: Firstly, A point load, F, would be applied directly on the shaft. Secondly two forces, $\frac{F}{2}$, would be applied to the disks at the hydraulic radius on opposing sides of the shaft; one negative and one positive, as seen in figure 3.27b). The latter describes a less conservative load scenario, hence the usage of the one in figure 3.27a). In addition, the load could have been applied with an angle to the disk. This would replicate the angle αbetween the flow from the nozzle and the runner.

Mesh and elements

A fairly coarse mesh was chosen. A finer mesh could be made and potentially acquire better results, but the decision was made to keep the mesh coarse for three reasons.

Firstly, the loads supplied by RHL are very approximate. A very accurate result obtained from approximate loads would not necessarily add to the quality of the evaluation.

Secondly, the purpose of the analyses was to compare the results from the various models to each other. It was then more important to ensure a similar mesh density for all models. The cavity models were also meshed with similar densities at the cavities.

Finally, a mesh with relatively low density requires less run time for the analyses. This makes it possible to run such analyses on a computer with a relatively low capacity within reasonable time. This could be of use to RHL. The density of the mesh can be seen in Appendix D.

Constraints and boundary conditions

The way the bearings are simulated are not completely analogous to the actual, physical case. A more accurate way to simulate this would be to model the bearing from the drawings, adding it to the assembly and applying the correct contact constraints to both shaft and bearing. Using the structural distributing coupling as presented in figure 3.23, the shaft is allowed to move in a very similar manner, seeing as the deformations in our analyses are quite small. The stresses around the bearing were not of particular importance in our assessment either.

The boundary condition used to simulate the influence of the turbine blades is not completely analogous to the physical case. The blades themselves would deform as well as introducing a different stress state of the attachment area on the disks, the effects would most likely not be very significant closer to the weld. Introducing blades to the model would be substantially more time consuming in both modelling, meshing and analysis. The blades hindering the disk ends from moving in the Z-direction is assumed to be the most prominent effect, which was honoured by the boundary condition, Zsymm.

Loads

Alternatively, the loads could be applied to the disks as seen in figure 3.27b). This describes, as mentioned, a less conservative load scenario,

hence the usage of the one in figure 3.27a). The load was chosen to be modelled as in a), because of the more conservative configuration.

Results

The stresses found around the weld in figure 4.3 for the configuration without bushing are significantly higher compared to figure 4.4 with bushing. The maximum stresses are as low as 18 MPa for the 1 pulley bushing model, meaning that the introduction of the bushing has reduced the maximum Von Mises stresses at the weld by 67 %.

For the 2 pulley models, the introduction of the bushing has reduced the maximum Von Mises stress from 51 to 33 MPa - 39 %. It has also moved the area of highest stress to the disk. The improvement will most likely do wonders for the fatigue life.

2D models

To make an estimate on the stress concentration in a potential cavity in the disk, the relative SCFs were calculated by dividing the cavity stress with the respective no cavity stress. Table 4.3 on page 65 has been expanded below.

Side of weld toe	No cavity	Cavity	SCF
Bushing	2,7 MPa	5,9 MPa	2,16
Disk	20 MPa	73 MPa	4,47

Table 5.1: Relative SCFs from the 2D analyses.

The ratio between the two relative SCFs is at 2,07. The results from the 3D models give a SCF of approximately 4 for the 2 pulley bushing cavity model. Multiplying the two gives a *very* rough estimate of 8,14 for the SCF of a cavity in the disk at the 2 pulley model. Multiplying this fictive SCF with the disk stress of for the 3D model (4.4 on page 61), gives a cavity stress of 276 MPa. This is a very high stress that would drastically reduce the fatigue life. The authors wish to emphasise the roughness of

this approximation. It does, however, indicate that a cavity in the disk could be critical.

5.1.6 Fatigue life

The ultimate tensile strength for the bushing material is used for the whole structure in the case with bushing, even though the bushing only encloses the shaft. This is a conservative assumption, as the shaft material is more resistant to fatigue fracture. If a fatigue limit had been available, the stress amplitude for the case with bushing would definitely be below, as the stress amplitudes are 14 and 26 times lower than the tensile strength.

A better model, and more data from the turbines suffering from fatigue fracture are needed to establish a reliable fatigue limit.

The S-N curve slope parameter b is found to be -0,183 based on equation 4.11 on page 68. This is justified by Härkegård [8, sec. 2.3.1] stating with macroscopic material and welding defects, the number could be between -0,2 and -0,3. The value obtained is a result of very uncertain inputs;

- A statement from RHL that many turbins break after one year of service.
- A statement from RHL that the average net head was 7 meters for the broken turbines.
- The turbine could have had macroscopic defects.

In addition, the number of cycles for the case with the broken shaft are above 10^6 which normally are used as the fatigue limit. The guess is that the shaft fractured because of different magnitudes of stress, with a few of these above the fatigue limit, a so-called Fatigue Damage Spectrum (FDS).

There is reason to believe that b = -0,813 is higher than the real situation. The fatigue life obtained with b = -0,13 and stress levels from FEA for the turbine with bushing, is unlimited for the 1 pulley configuration. The fatigue life for the 2 pulley case is 433 days. The number of cycles are well

above 10^6. With the rotors rotational speed of 832 rpm appropriate for 50 meters net head, 10^6 cycles are reached after one day of service. With that in mind, the decrease of stress level is more appropriate for determining whether the introduction of bushing is an improvement or not.

5.2 Conclusions

- The introduction of the bushing has substantially increased the fatigue life of HKT, however, potential cavities in the disk may, in fact, shorten it. Cavities must be avoided.
- The cavities and micro cracks found are a result of the welding. The method, procedure and welding material used needs to be revised. Most issues regarding the fatigue life of HKT are related to the welding.
- The quality of the materials is low, as predicted by RHL. The high number of inclusions may contribute to a shorter fatigue life.
- With the introduction of a bushing to the original design, the stress level decreases with at least 52,5% in the area previously subject to fatigue fracture.
- The test rod supplied by RHL is not of the same material as the shaft, contrary to the information we received initially.
- It is not possible to establish a fatigue limit with respect to stress amplitude based on the few fatigue data received. What can be said, is that the stress levels at the weld previously subject to fatigue fracture, has been reduced substantially with the introduction of bushing.

Bibliography

[1] Remote Hydrolight. Remote hydrolight website, May 2013.

[2] Eve Cathrin Walseth. Investigation of the flow through the runner of a cross-flow turbine, 2009.

[3] Howard E. Boyer. *Atlas Of Fatigue Curves*. ASM International, 1986.

[4] P. Verhaart. Blade calculations for water turbines of the banki type. Technical report, Eindhoven University of Technology, 1983.

[5] P. Zhang, S.X. Li, and Z.F. Zhang. General relationship between strength and hardness. *Materials Science and Engineering A*, 529(10):63–73, November 2011.

[6] Ian Scales. Cross-flow turbine design. *Soft Technology*, (35), 1990.

[7] Jack A. Collins, Henry Busby, and George Staab. *Mechanical Design of Machine Elements and Machines*. John Wiley & Sons, 2 edition, 2009.

[8] Gunnar Härkegård. *Dimensjonering av Maskindeler*. tapir akademisk forlag, 2004.

[9] Michael E. Plesha Robert D. Cook, David S. Malkus and Robert J. Witt. *Concepts and Applications of Finite Element Analysis*. John Wiley & Sons Inc., 2002.

[10] AWS A5 Committee on Filler Metals and Allied Materials. Specification for carbon steel electrodes for shielded metal arc welding. Standard, American Welding Society, 2004.

[11] Hobart Institute of Welding Technology. Guidelines for shielded metal arc welding (smaw). Instruction manual, Miller Electric Mfg. Co., 2013.

[12] Senior Principal Engineer at Det Norske Veritas Bjø rn Andreas Hugaas. Metallurgic consultation. Conversation, image inspection. Evaluation of metallographic images taken by the authors.

[13] Anders Austegard. Headflowdiagram. Excel sheet. Calculations done by Remote Hydrolight.

[14] Warren C. Young and Richard G. Budynas. *Roarks Formulas for Stress and Strain.* McGraw-Hill, 7 edition, 2002.

Appendix A

Net head - Flow diagram

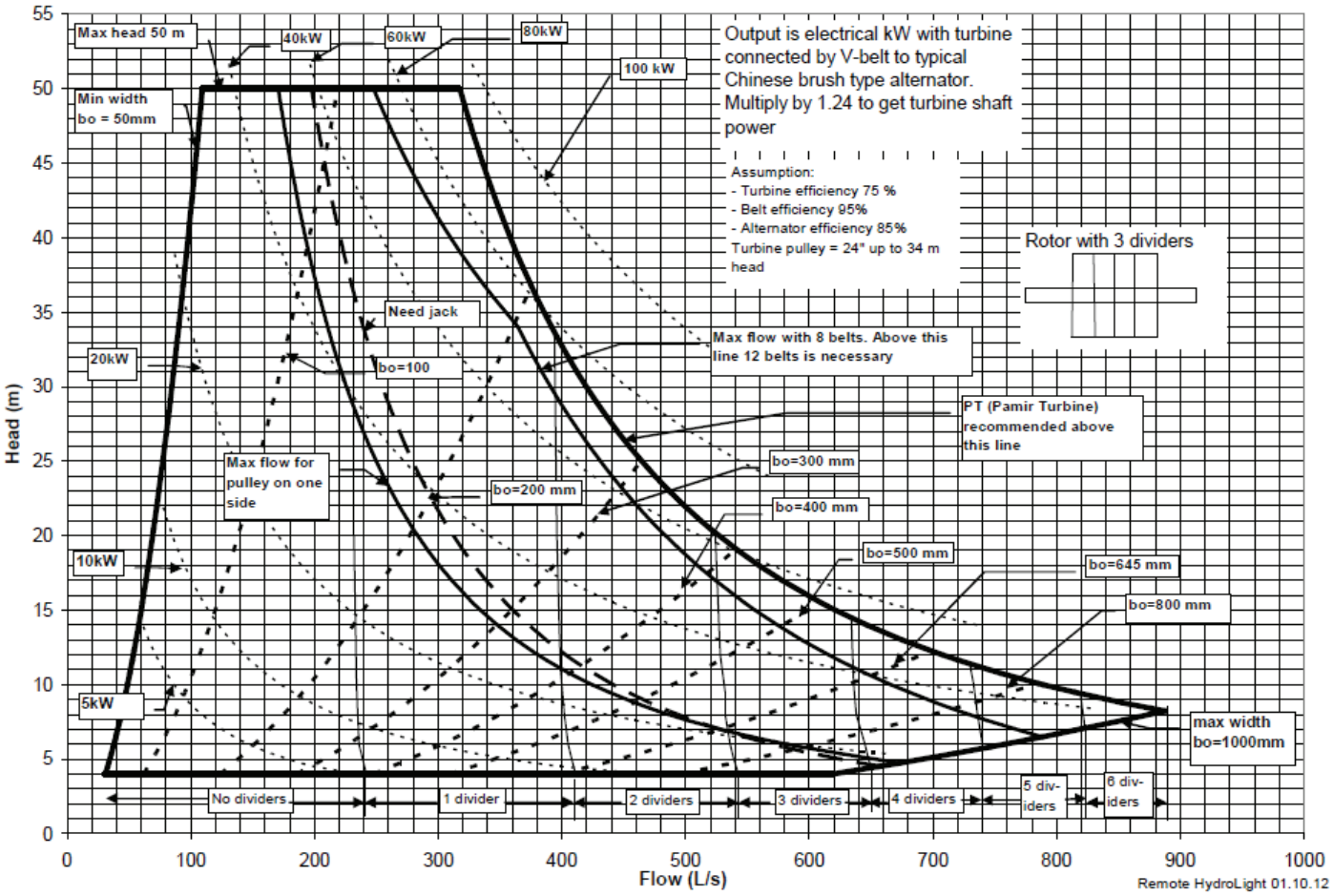

Appendix B

Technical Drawings

B.1 Shaft with disks

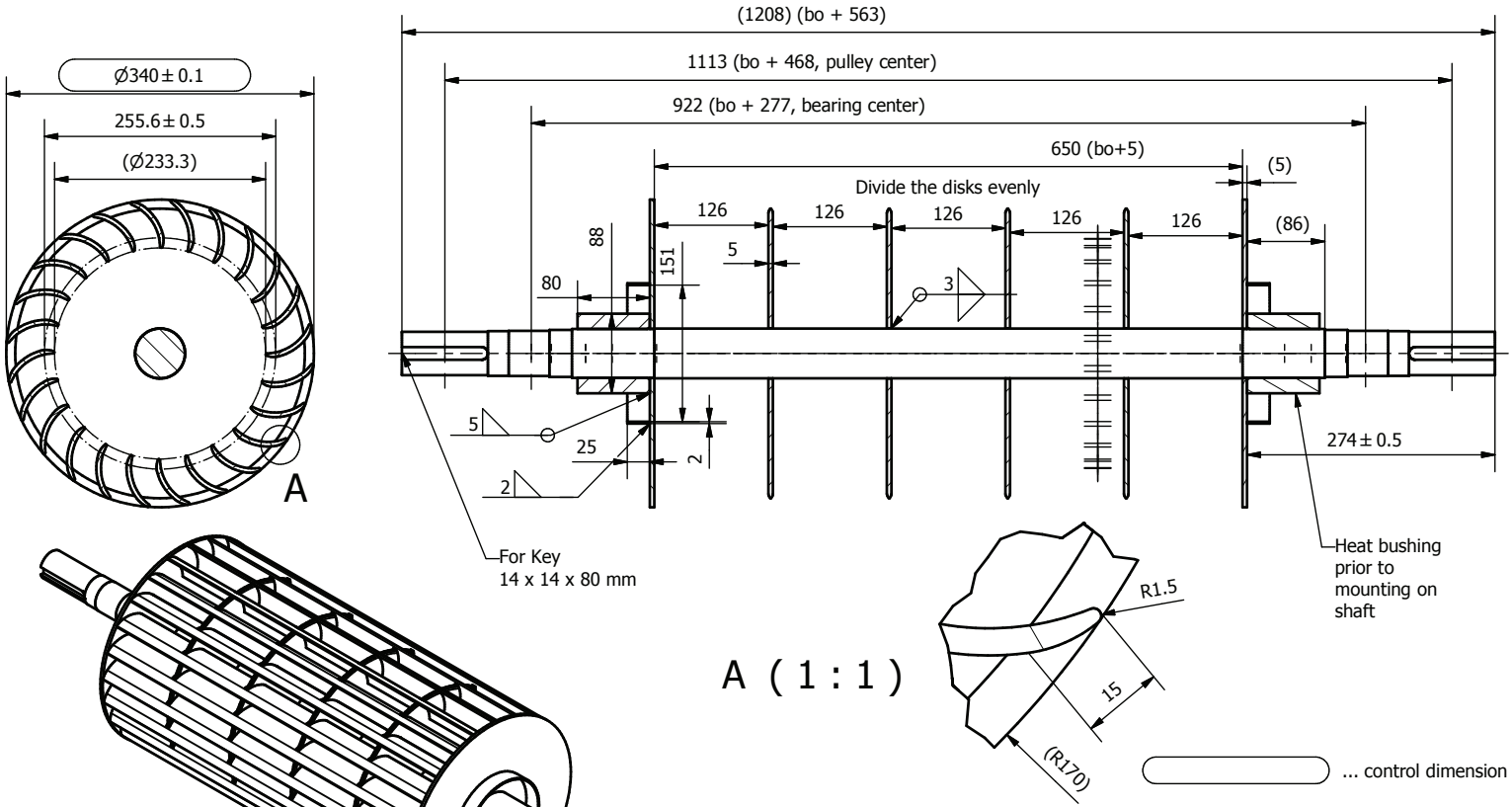

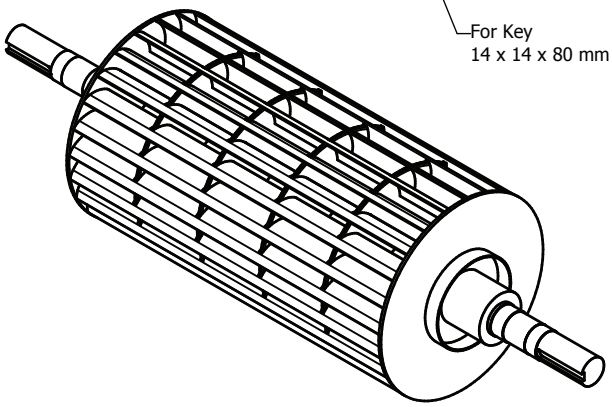

Format A4	RHL/IAM		
Date	01/10/2012	Runner - for HKT-645	
Material			
1 (632.100.000) Runner.idw		1.H6	2 / 5
	632.100.000		
Turbine	HKT-645	This drawing is the propety of Remote HydroLight and IAM, Afghanistan	

B.2 Shaft dimensions

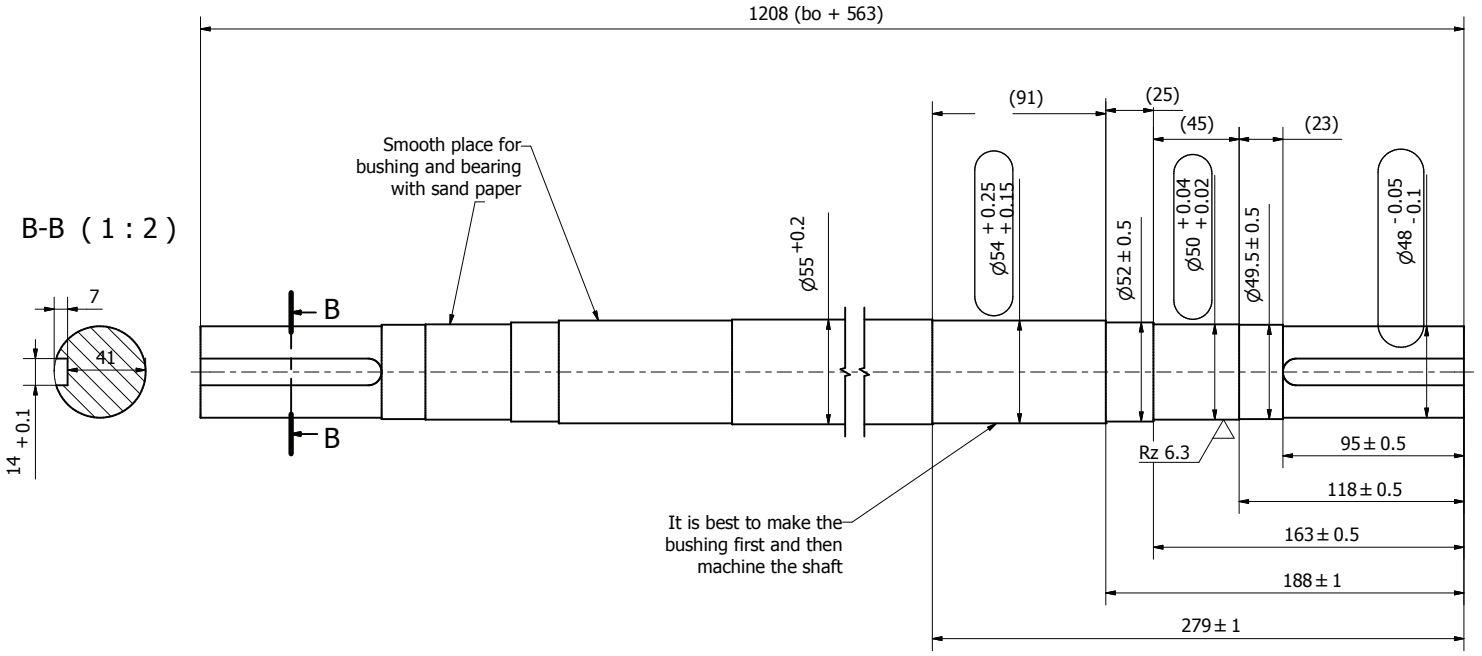

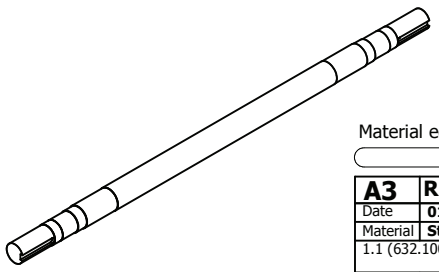

Material equivalent to SAE 1045

... control dimension

A3	**RHL/IAM**	
Date	**01/10/2012**	**Shaft - With keyway**
Material	**Steel, Mild**	
1.1 (632.100.001) Shaft.idw		
665.100.001		**1.1.H6** **1 / 1**
Turbine	**HKT-645**	This drawing is the propety of Remote HydroLight and IAM, Afghanistan

B.3 Disk

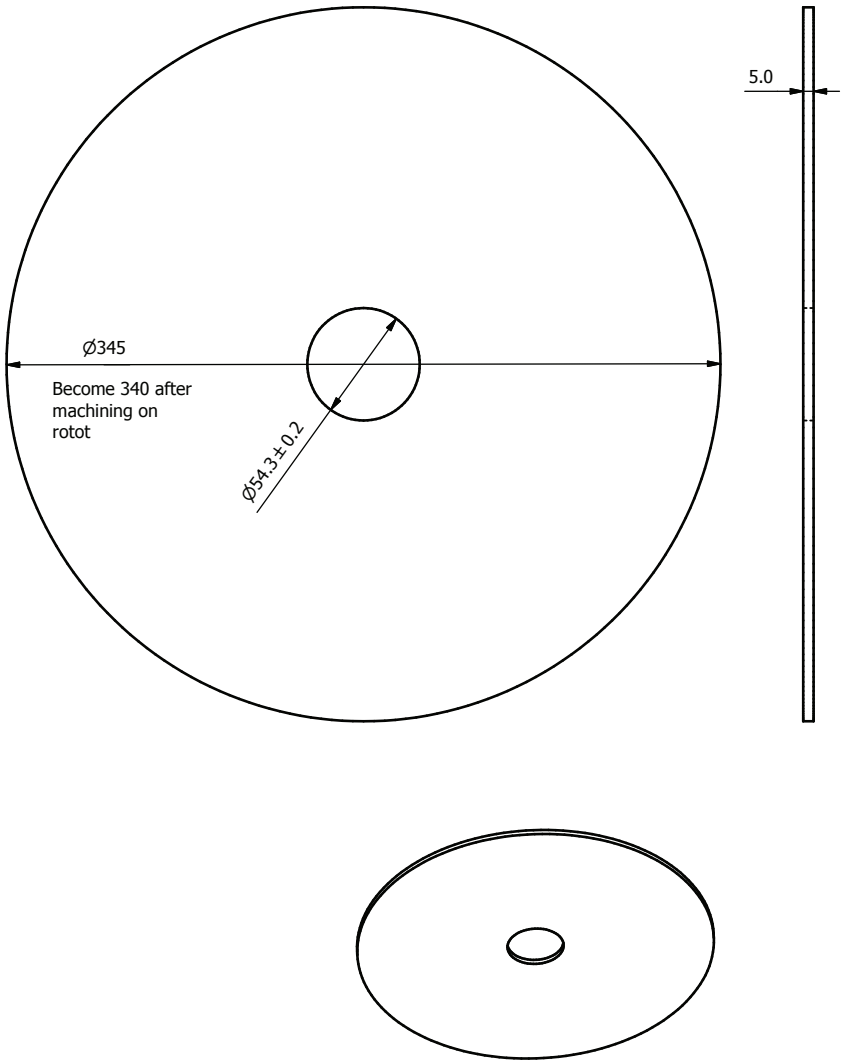

Format **A4**	**RHL/IAM**	**Disk before machining on rotor**
Date	**18/08/2012**	**Disk - For rotor side**
Material	**Steel, Mild**	
1.3 (665.100.003) Disk-side.idw	665.100.003	**1.3.H** **1 / 1**
Turbine	**HKT-645**	This drawing is the propety of Remote HydroLight and IAM, Afghanistan

Appendix C

Velocity equations

Input;

c_1 Absolute inlet flow velocity

α_1 Inlet absolute flow angle

α_2 Outlet absolute flow angle stage 1

β_1 Relative flow angle inlet

β_2 Relative flow angle outlet stage 1

$\Psi = 2$ Work coefficient, assumed impulse turbine under atmospheric pressure

R_o Radius from centre of rotor to outer tip of blades

R_i Radius from centre of rotor to inner tip of blades

$$u_1 = \frac{c_1 \cos(\alpha_1)}{\Psi} \tag{C.1}$$

$$w_1 = \frac{c_1 \cos(\alpha_1) - u_1}{\sin(90^\circ - \beta_1)} \tag{C.2}$$

$$u_2 = u_1 \frac{R_i}{R_o} \tag{C.3}$$

$$w_2 = w_3 = u_2 \tan(\alpha_2) \tag{C.4}$$

$$c_2 = c_3 = \sqrt{u_2^2 + w_2^2} \tag{C.5}$$

$$u_4 = u_1 \tag{C.6}$$

$$w_4 = w_1 \tag{C.7}$$

Appendix D

Colour plots from FEA

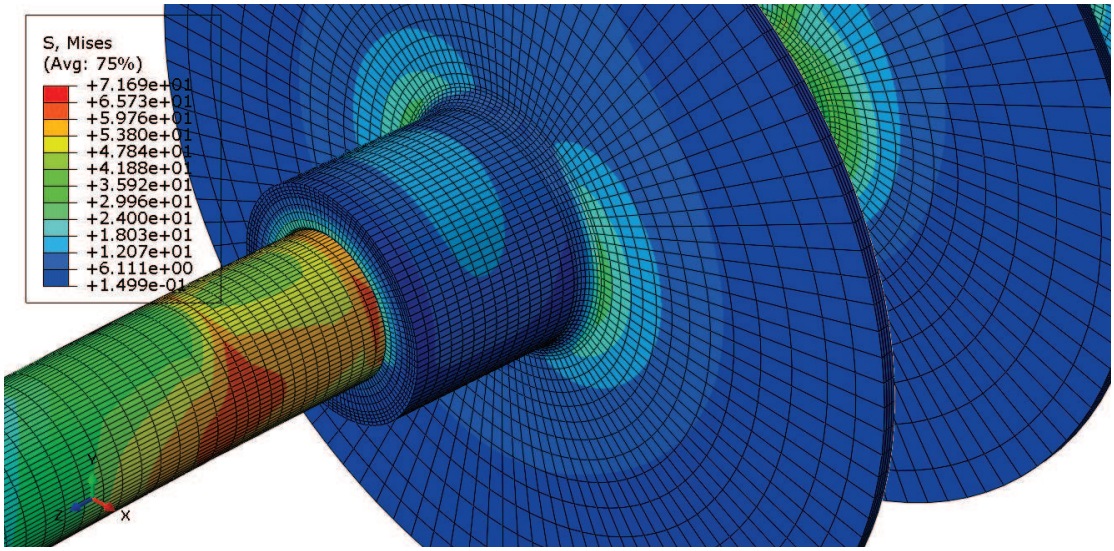

Figure D.1: 2 pulleys bushing model

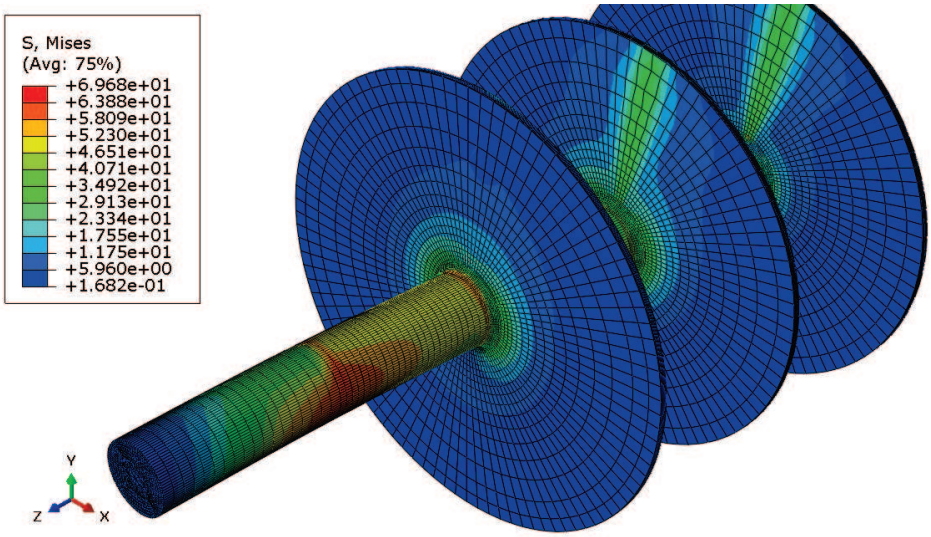

Figure D.2: 2 pulleys model, without bushing

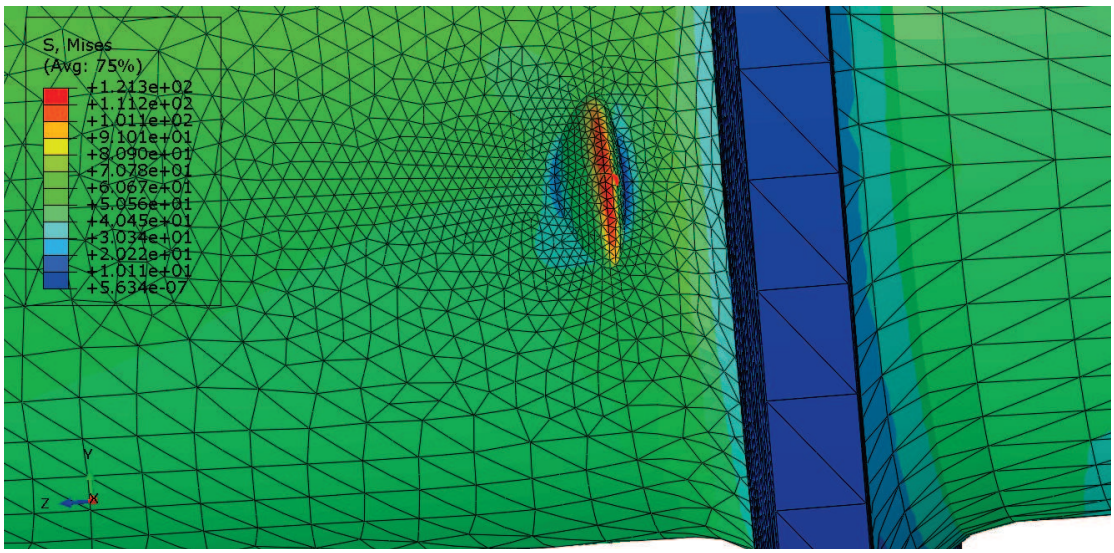

Figure D.3: 1 pulley cavity model, without bushing

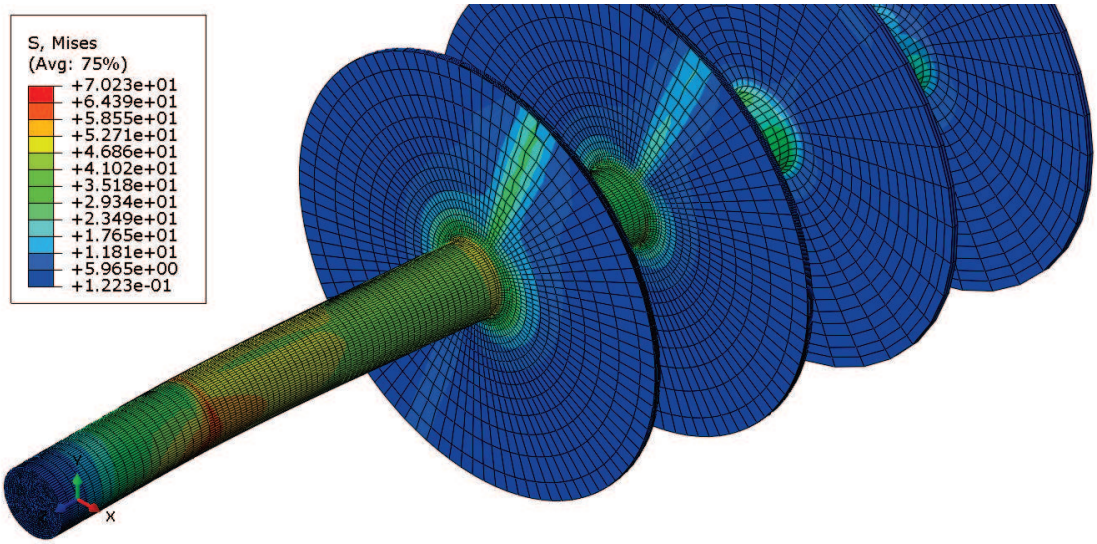

Figure D.4: 1 pulley broken bushing model

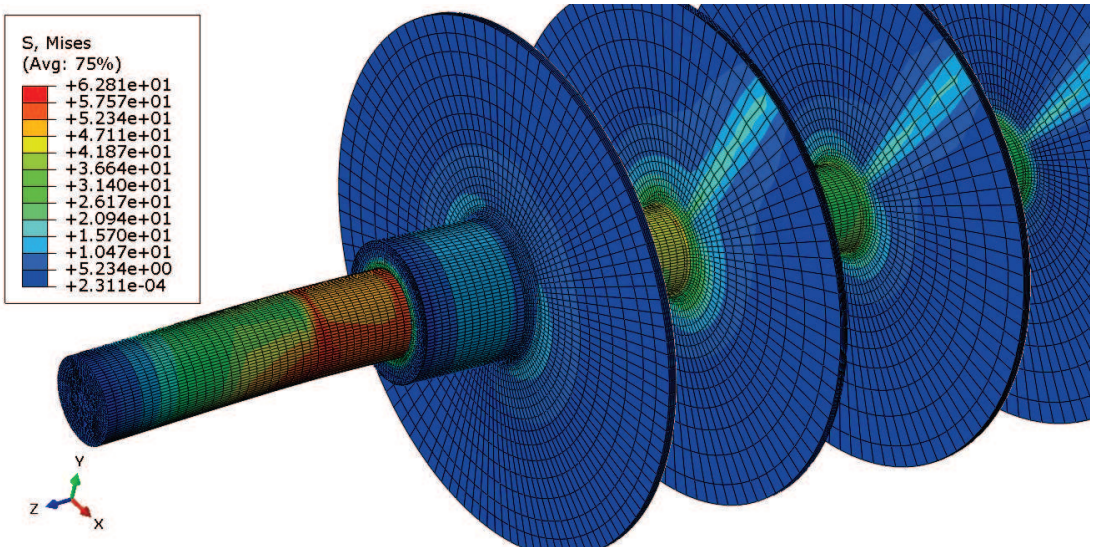

Figure D.5: 1 pulley bushing model

Appendix E

Digital appendix

E.1 Torque distribution on blades

torqueblades.m

E.2 Force calculations

Forcecalculations rotor.ods